

Disc instability and bar formation: view from the IllustrisTNG simulations⁵

David Izquierdo-Villalba,^{1,2*} Silvia Bonoli,^{3,4} Yetli Rosas-Guevara,³ Volker Springel,⁵ Simon D.M. White,⁵ Tommaso Zana,⁶ Massimo Dotti,^{1,2,7} Daniele Spinoso,^{3,8} Matteo Bonetti,^{1,2,7} Alessandro Lupi^{1,2}

¹Dipartimento di Fisica “G. Occhialini”, Università degli Studi di Milano-Bicocca, Piazza della Scienza 3, I-20126 Milano, Italy

²INFN, Sezione di Milano-Bicocca, Piazza della Scienza 3, 20126 Milano, Italy.

³Donostia International Physics Centre (DIPC), Paseo Manuel de Lardizabal 4, 20018 Donostia-San Sebastian, Spain

⁴IKERBASQUE, Basque Foundation for Science, E-48013, Bilbao, Spain

⁵Max-Planck Institute for Astrophysics, Karl-Schwarzschild-Str. 1, D-85741 Garching, Germany

⁶Scuola Normale Superiore, Piazza dei Cavalieri 7, I-56126 Pisa, Italy

⁷INAF, Osservatorio Astronomico di Brera, Via E. Bianchi 46, I-23807, Merate, Italy

⁸Centro de Estudios de Física del Cosmos de Aragón (CEFCA), Plaza San Juan 1, Planta-2, Teruel, 44001, Spain.

Accepted XXX. Received YYY; in original form ZZZ

ABSTRACT

We make use of $z=0$ samples of strongly barred and unbarred disc galaxies from the TNG100 and TNG50 cosmological hydrodynamical simulations to assess the performance of the simple disc instability criterion proposed by Efstathiou, Lake & Negroponte (1982) (ELN-criterion). We find that strongly barred galaxies generally assemble earlier, are more star-dominated in their central regions, and have more massive and more compact discs than unbarred galaxies. The ELN-criterion successfully identifies $\sim 75\%$ and $\sim 80\%$ of the strongly barred and the unbarred galaxies, respectively. Strongly barred galaxies that the criterion fails to identify tend to have more extended discs, higher spin values and bars that assembled later than is typical for the bulk of the barred population. The bars in many of these cases appear to be produced by an interaction with a close neighbour (i.e. to be externally triggered) rather than to result from secular growth in the disc. On the other hand, we find that unbarred galaxies misclassified as barred by the ELN-criterion typically have stellar discs similar to those of barred galaxies, although more extended in the vertical direction and less star-dominated in their central regions, possibly reflecting later formation times. In addition, the bulge component of these galaxies is significantly more prominent at early times than in the strongly barred sample. Thus, the ELN-criterion robustly identifies secular bar instabilities in most simulated disc galaxies, but additional environmental criteria are needed to account for interaction-induced bar formation.

Key words: methods: numerical – galaxies: bar – galaxies: disc – galaxies: formation

1 INTRODUCTION

Nowadays we know that bars are common structures of galaxies in the local Universe where nearly 60 percent of the disc dominated galaxies host one (Knapen 1999; Eskridge et al. 2000; Grosbøl et al. 2004; Menéndez-Delmestre et al. 2007; Barazza et al. 2008a). Bars are believed to be important for the secular evolution of disc-dominated galaxies. Their capability of redistributing the galaxy angular momentum leads to gas inflows towards the galaxy nuclei, triggering star formation episodes which ultimately can lead to the formation of a pseudobulge (Lynden-Bell & Kalnajs 1972; Tremaine & Weinberg 1984; Kormendy 1993; van Albada & Roberts 1981; Schwarz 1981; Sakamoto et al. 1999). Even though current simulations are able to track the evolution of stellar discs (Navarro & Benz 1991; Navarro & Steinmetz 2000), it remains unclear why certain galaxies end up developing a bar structure whereas other similar galaxies do not. One of the pioneering works trying to shed light

on the physical conditions that lead to bar formation was Efstathiou et al. (1982), which explored the global stability of cold exponential stellar discs by performing a set of 2D N-body simulations. Interestingly, the authors found a simple analytical definition to determine the stability against bar formation:

$$\epsilon = \frac{V_{\max}}{(GM_{\text{disc}}/R_d)^{1/2}} \quad (1)$$

where G is the gravitational constant, V_{\max} is the maximum rotational velocity of the system, R_d is the scale length of the stellar disc and M_{disc} its total mass. The simulations showed that galaxies with $\epsilon > 1.1$ possess a large enough hot component able to stabilize the stellar disc. Instead, galaxies with $\epsilon \leq 1.1$ have stellar discs that become bar unstable. Thanks to the simplicity of the criterion (ELN-criterion hereafter), years later Mo et al. (1998a) adopted it to build a phenomenological model of disc galaxy formation within a hierarchical galaxy formation model.

Subsequent works addressing the bar formation process focused on the role of the dark matter (DM) component. Unlike Efstathiou

* E-mail: david.izquierdovillalba@unimib.it

et al. (1982), they included *live* DM halos that are capable to interact dynamically with the stellar structure (see e.g. Debattista & Sellwood 1998; Holley-Bockelmann et al. 2005; Weinberg & Katz 2007a,b; Romano-Díaz et al. 2008; Dubinski et al. 2009; Saha & Gerhard 2012). Athanassoula & Misiriotis (2002) compared two numerical simulations of isolated galaxies with the same disc-to-halo ratio, showing that the galaxy with larger halo concentration developed a much stronger, larger and thinner bar. Besides, Debattista & Sellwood (1998), Debattista & Sellwood (2000) and Athanassoula (2003) showed that halo concentration can leave an imprint on the bar strength and pattern speed. On top of concentration, the total halo mass in which a galaxy reside might play an important role as well. By performing numerical simulations, Athanassoula (2003) showed that while the most massive halos hosted the systems with the strongest bars, the less massive ones displayed weaker bar structures. During the last years, many studies have focused also on the effect of the halo spin in the stability of the stellar disc against bar modes. Saha & Naab (2013) reported that dark matter halos with a spin parameter between 0 and 0.07 in co-rotation with the stellar disc are able to prompt the formation of bars and boxy bulges. Long et al. (2014) found the opposite trend, showing that bar formation in spinning dark matter halos might be heavily suppressed. Along the same line, Collier et al. (2018) showed that bars hosted in halos with the largest spin had difficulties in re-growing bars after a buckling instability. Even more, in many cases bars were dissolved, leaving behind a host disc with large radial dispersion velocities. The authors attributed this bar dumping to the difficulty of spinning DM halos to absorb additional angular momentum.

On top of the dark matter component, the bulge one can play a major role in the bar assembly and evolution (Ostriker & Peebles 1973). For instance, Kataria & Das (2018) using N-body simulations of isolated galaxies, showed a delay in the bar formation as a function of the galaxy bulge-to-disc ratio (B/D). Particularly, they reported a B/D upper cut off above which the development of a bar is suppressed. While in dense bulges this cut was at $B/D \sim 0.2$, in the less dense ones was at $B/D \sim 0.5$ (see also the work of Kataria et al. 2020). Similar dependencies with the bulge prominence could be derived by the comparison of the twins zoom-in hydrodynamical simulations *Eris* and *ErisBH* (Guedes et al. 2011; Bonoli et al. 2016), where the bar structure developing only in *ErisBH* is likely favoured by the smaller bulge of this galaxy with respect to the one of *Eris* (Spinoso et al. 2017). Some observational studies have also shown a correspondence between the presence of bulges and bars. For instance, the results of Barazza et al. (2008b) and Aguerri et al. (2009) pointed out that the bar fraction decreases with increasing bulge luminosity.

During the last years, semi-analytical models (SAMs) have tried to shed light on the evolution of barred galaxies inside a hierarchical universe. For that, they have generally relied on the aforementioned ELN-criterion, which has the advantage of being simple and depending only on global galaxy properties, easily accessible in SAMs (Guo et al. 2011; Barausse 2012; Croton et al. 2016; Lacey et al. 2016; Cora et al. 2018). Although the ELN-criterion does not take into account all the dependencies discussed above (see the discussion of Athanassoula 2008), SAM predictions display, in general, a good agreement with observations (see for instance Izquierdo-Villalba et al. 2019; Irodotou et al. 2019; Marshall et al. 2019). Despite its important role in this context, no systematic study about the performance and reliability of the ELN-criterion in a cosmological context has done to date. Some attempts in this

direction can be found in Yurin & Springel (2015), who explored the performance of the ELN-criterion by using a methodology to include live stellar discs into high-resolution Milky Way-like dark matter halos. Interestingly, the authors reported that the ELN-criterion should be taken as an important first guide to discriminate between bar stable or unstable discs. Simulations of isolated dark matter halos with an embedded stellar disc performed by Mayer & Wadsley (2004) pointed towards the same direction. Even more, the authors suggested that the disc-to-halo ratio within the typical disc radius might be the main factor determining the final development of barred structures (see similar results of DeBuhr et al. 2012). Even though these works are important for supporting the ELN-criterion as a necessary condition for bar formation, they could not test its performance with a large galaxy sample, evolving consistently in their full cosmological context. Such tests are now possible thanks to the latest generation of cosmological hydrodynamical simulations, which can currently follow the physical assembly of galaxies down to relatively small scales in representative cosmological volumes (see e.g. Dubois et al. 2014; Schaye et al. 2015; Nelson et al. 2018; Davé et al. 2019). Indeed, it has been shown that current cosmological hydrodynamical simulations are capable to reproduce the barred galaxy population at $z=0$ (see Algorry et al. 2017, EAGLE, Peschken & Lokas 2019, Illustris, Rosas-Guevara et al. 2020, 2021, IllustrisTNG, Reddish et al. 2021, NewHorizonAGN, Fragkoudi et al. 2021, AURIGA), even though some tensions still remain (see e.g. Fragkoudi et al. 2021; Roshan et al. 2021).

In this paper we systematically explore, for the first time, the performance of the Efstathiou et al. (1982) analytical criterion using a sample of barred and unbarred galaxies extracted from a large cosmological hydrodynamical simulation. In particular, we focus on $z=0$ Milky-Way type galaxies ($10^{10.4} M_{\odot} \lesssim M_{\text{stellar}} \lesssim 10^{11} M_{\odot}$) extracted from the TNG100 and TNG50 simulations. The outline of this work is as follows. In Section 2 we describe the main characteristics of the TNG100/TNG50 simulations and the barred/unbarred galaxy sample. Besides, we present our methodology to extract the stellar disc scale length. In Section 3 we analyse the general properties of barred and unbarred galaxies. In Section 4 we test the success rate of the ELN-criterion, we study the characteristics of correctly and incorrectly classified barred/unbarred galaxies. Finally, in Section 5 we summarize our main findings. A Lambda Cold Dark Matter (Λ CDM) cosmology with parameters $\Omega_m = 0.309$, $\Omega_{\Lambda} = 0.691$, $\Omega_b = 0.047$, $\sigma_8 = 0.816$ and $H_0 = 67.74 \text{ km s}^{-1} \text{ Mpc}^{-1}$ is adopted throughout the paper (Planck Collaboration et al. 2016). Unless explicitly stated, all the distances used in this work are physical distances.

2 THE GALAXY SAMPLE

In this section we present our sample of simulated barred/unbarred galaxies, extracted from the *The Next Generation Illustris Simulations*¹ (hereafter, TNG, Nelson et al. 2019a). Specifically, we make use of TNG100 and TNG50 whose volume, mass and spatial resolution guarantees a good sampling of massive disc-dominated galaxies (see e.g. Rosas-Guevara et al. 2020; Du et al. 2019; Zhou et al. 2020; Rosas-Guevara et al. 2021; Gargiulo et al. 2021). Among the entire galaxy population, we focus on $z=0$ Milky-Way

¹ The simulations of the TNG project are available at <https://www.tng-project.org/> (Nelson et al. 2019a)

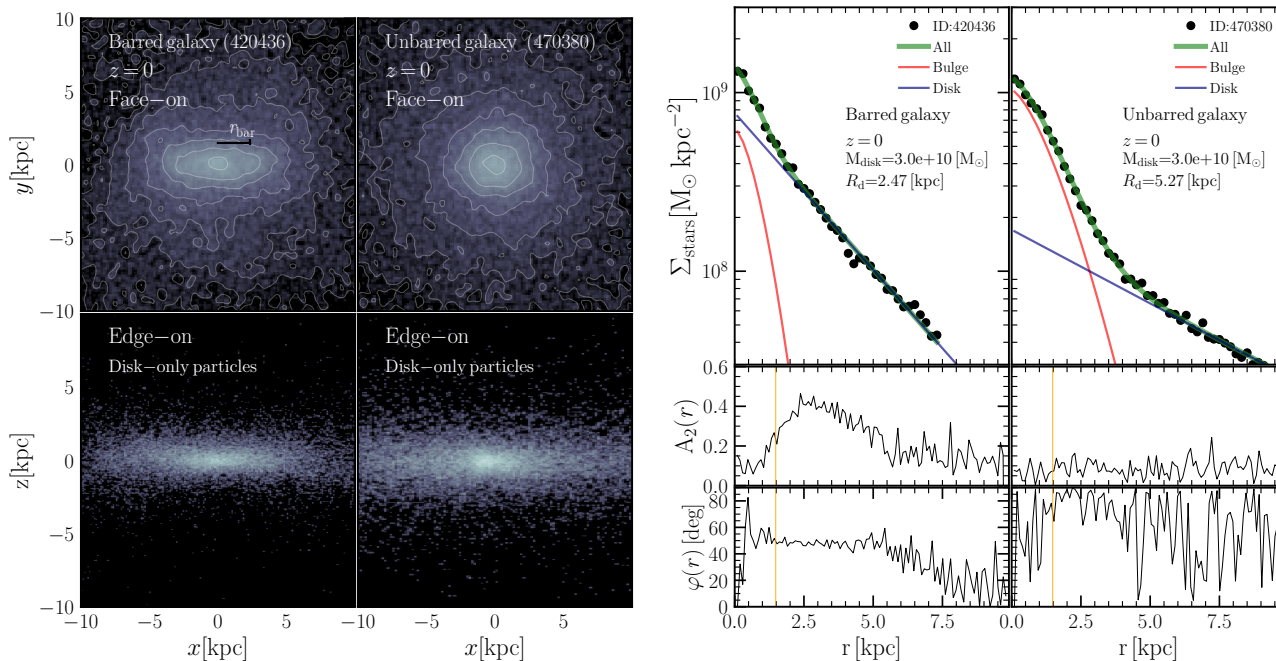


Figure 1. **Left panel:** Galaxy face-on (up) and edge-on (down) surface mass density maps for a TNG100 barred (left) and TNG100 unbarred (right) galaxy at $z=0$. For the edge-on view we only show the disc particles (see Eq. 7). **Right panel:** The upper panels display the galaxies (barred left and unbarred right) face-on surface density profile: pink, red and green represent, respectively, the fit of the whole galaxy, the bulge and the disc component. The middle and lower panels show the value of $A_2(r)$ and $\varphi(r)$, respectively. To guide the reader, the vertical orange lines highlight the position at which r is equal to twice the softening length of TNG100 at $z=0$.

type galaxies ($10^{10.4} \lesssim M_{\text{stellar}} \lesssim 10^{11} M_{\odot}$ and disc-to-total ratio, $D/T > 0.5$) which have proved to be the preferential hosts and birth-places of bar structures in the low- z Universe (see e.g. Gadotti 2009; Cervantes Sodi et al. 2015; Gavazzi et al. 2015; Izquierdo-Villalba et al. 2019; Marshall et al. 2019).

2.1 IllustrisTNG project

The TNG project is a set of simulations of large cosmological volumes run with the moving-mesh code AREPO (Springel 2010). To follow the evolution of galaxies and subhalos, AREPO solves the magneto-hydrodynamics equations coupled with self-gravity and includes an updated version of the Illustris² subgrid galaxy physics (Vogelsberger et al. 2014b,a). The subgrid model includes prescriptions for radiative gas cooling, stellar evolution, AGN/supernovae feedback, chemical enrichment, gas recycling, black hole seeding, black hole growth and metal loading of outflows (see further details in Weinberger et al. 2017; Pillepich et al. 2018a).

The TNG project is made up of three different simulation volumes (TNG300, TNG100 and TNG50) evolved from $z=127$ down to $z=0$ with cosmological parameters from Planck Collaboration et al. (2016). Among the three volumes, TNG100 (Pillepich et al. 2018b; Springel et al. 2018; Nelson et al. 2018; Naiman et al. 2018; Marinacci et al. 2018) follows in a 75Mpc/h comoving box size the evolution of 2×1820^3 dark matter particles and gas cells with mass of $7.46 \times 10^6 M_{\odot}$ and $1.39 \times 10^6 M_{\odot}$, respectively. At $z=0$,

the softening length of collisionless particles and gas component corresponds, respectively, to 0.5kpc/h and 125pc/h. On the other hand, TNG50 (Nelson et al. 2019b; Pillepich et al. 2019) simulates a smaller volume (35Mpc/h box size) but follows dark matter and gas using 2160^3 elements each, with masses of $4.5 \times 10^5 M_{\odot}$ and $8.5 \times 10^4 M_{\odot}$. By $z=0$, the softening length of collisionless particles and gas component corresponds to 0.195kpc/h and 50pc/h, respectively. Particle data of both TNG100 and TNG50 were stored in 100 different snapshots from $z \sim 20$ to $z=0$. Dark matter subhalos and galaxies were identified within these snapshots by using a friend-of-friend group finder (Davis et al. 1985) and the SUBFIND algorithm (Springel et al. 2001). Finally, by applying L-HALOTREE and SUBLINK algorithms (Springel 2005; Rodriguez-Gomez et al. 2015) all DM subhalos and galaxies were arranged in merger tree structures.

2.2 Bar and unbarred galaxies in TNG100 and TNG50

In this work we make use of the $z=0$ TNG100/TNG50 barred and unbarred galaxy sample of Rosas-Guevara et al. (2020) and Rosas-Guevara et al. (2021). For the TNG100 simulation, Rosas-Guevara et al. (2020) selected a $z=0$ galaxy sample with disc-to-total ratio (D/T) > 0.5 , guaranteeing morphologies fully dominated by the disc structure. To ensure a well-resolved disc, the extra condition of more than 10^4 stellar particles within twice the galaxy half mass radius (R_{half}) was also imposed. Such a particle limit sets a lower stellar mass cut of $M_{\text{stellar}} \sim 10^{10.4} M_{\odot}$. From this disc-dominated galaxy sample, the authors identified stellar bars via a Fourier decomposition of the face-on stellar surface density (Σ_{stars} , Athanassoula & Misiriotis 2002; Valenzuela & Klypin 2003). Specifically, they determined the strength of a non-axisymmetric nuclear compo-

² <https://www.illustris-project.org/>

ment (A_2) by computing the ratio between the second and zero terms of the Fourier expansion:

$$A_2(r) = \frac{|\sum_j M_j e^{2i\theta_j}|}{\sum_j M_j}, \quad (2)$$

where M_j , θ_j , and r are the mass, angular coordinate in the galactic plane and radial distance of the j -th stellar particle, respectively. The sums of Eq. 2 were performed over all particles within cylindrical shells of 0.12 kpc width and 2 kpc height. In short, $A_2(r)$ displays an increasing trend up to a distance r_{\max} where the strength of the non-axisymmetric structure exhibits a maximum (A_2^{\max}). After r_{\max} , the values of $A_2(r)$ gradually decrease to zero. The position r_{\max} was used as an estimate of the bar length (r_{bar}). Finally, to avoid confusion between bars and other non-axisymmetric structures such as spiral arms (or spurious detection), the authors imposed that the phase of the second Fourier mode (see Zana et al. 2019):

$$\varphi(r) = \frac{1}{2} \arctan \left[\frac{\sum_j M_j \sin(2\theta_j)}{\sum_j M_j \cos(2\theta_j)} \right] \quad (3)$$

has to be constant within the bar length. This Fourier decomposition allowed Rosas-Guevara et al. (2020) to divide the disc dominated galaxy sample in three different groups: *unbarred sample* ($A_2^{\max} < 0.2$), *weak bar sample* ($0.2 \leq A_2^{\max} < 0.3$) and *strong bar sample* ($A_2^{\max} \geq 0.3$). As an example, in Fig. 1 we show the $A_2(r)$ and $\varphi(r)$ profiles for a strong barred and unbarred galaxy in TNG100. In what follows, among all the TNG100 galaxies selected by Rosas-Guevara et al. (2020), we only study the unbarred sample and strong bars (hereafter *barred sample* or *barred galaxies*). As reference, the total number of barred and unbarred galaxies is respectively 58 and 131, spanning a range in stellar masses between $10^{10.4} M_\odot$ and $10^{11} M_\odot$ ³.

To extract a disc galaxy sample in TNG50, Rosas-Guevara et al. (2021) applied a similar methodology to the one used for TNG100. Given the better mass resolution, the authors extended their analysis down to $M_{\text{stellar}} = 10^{10} M_\odot$, finding 349 disc dominated galaxies at $z=0$ of which 105 displayed $A_2^{\max} > 0.2$. Since our purpose is to compare TNG100 and TNG50 predictions and to explore how they vary with the resolution of the simulation, among all the disc galaxies of Rosas-Guevara et al. (2021), we only select the ones with $M_{\text{stellar}} (< 2R_{\text{half}}) > 10^{10.4} M_\odot$ and $D/T > 0.5$. For the selection of the barred sample, an extra cut of $A_2^{\max} \geq 0.3$ was performed. The final catalogue of TNG50 contains respectively 39 and 31 barred and unbarred galaxies. As we can see, the ratio between the number of barred and unbarred galaxies is smaller in TNG100 than TNG50. Besides cosmic variance, this difference could be caused by the fact that TNG50 simulation finds a larger number of disc-dominated galaxies than the former one. Nevertheless, exploring such differences in detail goes beyond the scope of this paper.

Following Rosas-Guevara et al. (2020), in this work we define the bar formation (lookback) time, t_f^{bar} (and its corresponding redshift,

³ The parent sample of disc-dominated galaxies in the $10^{10.4} < M_{\text{stellar}} < 10^{11} M_\odot$ mass range satisfying the previous cuts contains 270 galaxies. We refer to Rosas-Guevara et al. (2020) for further details.

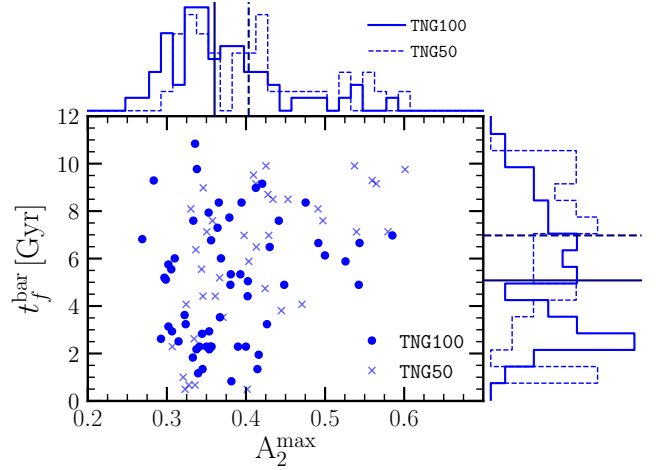


Figure 2. Left panels: Relation between the bar strength (A_2^{\max}) at $z=0$ and the bar formation time (t_f^{bar}) for TNG100 and TNG50 (circles and crosses, respectively). Upper and right histograms represent the distribution of A_2^{\max} and t_f^{bar} for TNG100 (solid lines) and TNG50 (dashed lines). Vertical lines display the median of the distributions.

z_f^{bar}), as the moment in which:

$$A_2^{\max}(t_f^{\text{bar}}) > 0.2 \quad \& \quad \frac{|A_2^{\max}(t_f^{\text{bar}}) - A_2^{\max}(t)|}{A_2^{\max}(t_f^{\text{bar}})} < 0.4, \quad (4)$$

where $A_2^{\max}(t)$ is the bar strength at the two simulation outputs before the bar formation. For unbarred galaxies we set their t_f^{bar} to the median value of the t_f^{bar} measured for the whole barred sample. Given that unbarred galaxies never develop a bar, this quantity does not have a physical meaning but it will serve us as a reference to compare with the barred sample. Finally, we also define a normalised time since bar formation, δt , computed as:

$$\delta t = \frac{t_f^{\text{bar}} - t_{\text{snp}}}{t_f^{\text{bar}}}, \quad (5)$$

where t_{snp} corresponds to the lookback time of the simulation snapshot. $\delta t = 0$ represents the bar formation time while $\delta t > 0$ ($\delta t < 0$) corresponds to times after (before) the bar formation. In Fig. 2 we present A_2^{\max} and t_f^{bar} at $z=0$ for barred galaxies in TNG100 and TNG50. As we can see, bar structures are slightly stronger and older in TNG50, which might be possibly due to resolution effects (Frankel et al. 2022). Regardless of these differences, we can see a weak trend of smaller bar strength at smaller t_f^{bar} . Besides, as reported by Rosas-Guevara et al. (2020), we find that the larger is the mass of the galaxy, the older is the bar structure (see Figure 6 of Rosas-Guevara et al. 2020).

2.2.1 Characterization of the disc properties

Given that the ELN-criterion depends on the stellar disc mass and its scale length (see Eq.1), we need to extract these quantities from our sample of disc-dominated galaxies. To do that, for each galaxy we calculate the angular momentum of the baryons⁴ (\vec{J}_{baryons}) and

⁴ We select only gas and stellar particles within 20kpc around the most bound particle of the galaxy.

rotate its reference system in such a way that we align \vec{J}_{barions} with the z-axis. After the rotation, we compute the galaxy stellar face-on surface density profile, $\Sigma_{\text{stars}}(r)$ and we fit it to a composite model obtained as the sum of a Sérsic model (Sersic 1968) and an exponential profile:

$$\Sigma_{\text{stars}}(r) = \Sigma_{\text{b}} e^{-b_n \left[\left(\frac{r}{R_{\text{b}}} \right)^{\frac{1}{n}} - 1 \right]} + \Sigma_0^{\text{d}} e^{-\frac{r}{R_{\text{d}}}}, \quad (6)$$

where the first and second term represent the bulge and disc component. Σ_{b} , R_{b} and n correspond to the central surface density, effective radius and Sérsic index of the bulge component. On the other hand, Σ_0^{d} and R_{d} are the central surface density and the scale length of the galaxy stellar disc. The b_n value is such as $\Gamma(2n) = 2\gamma(2n, b_n)$ where Γ and γ are, respectively, the *complete* and *incomplete* gamma function. The fits have been done by finding first the optimal parameters of the exponential disc profile and afterwards we model with the Sérsic profile the central residual excess, i.e the bulge (see the same approach performed in Scannapieco et al. 2011; Marinacci et al. 2014). We have used the kinematic bulge-to-disc decomposition of Genel et al. (2015) as an initial guess for the break at which the change between the exponential and the Sérsic law happens. These fits have been done up to $2R_{\text{half}}$ and throughout the whole cosmological evolution of the galaxy. In Appendix A we show that our R_{d} values are consistent with the ones obtained by only fitting the surface mass density of the thin disc structure, selected according to the kinematic decomposition of Zana et al. (submitted). As an example of the fit performance, in Fig. 1 we present the face-on stellar surface density profile and its disc-bulge decomposition for a barred and unbarred galaxy at $z=0$ in TNG100. As we can see, in both galaxies the structural decomposition finds a well behaved exponential declining trend corresponding to the galactic disc structure.

Another important property in the study of disc structure is the vertical scale length, z_{d} , which gives information about how stars are distributed perpendicularly to the disc (see e.g. Yoachim & Dalcanton 2006; Comerón et al. 2011). To determine the vertical length, in the reference system aligned with the z-direction, we separate stellar disc particles from the bulge ones by computing the particle circularity parameter, η (Abadi et al. 2003; Scannapieco et al. 2009; Marinacci et al. 2014):

$$\eta = \frac{J_{z,*}}{rv_c(r)} \quad (7)$$

where r is the star radial distance, $J_{z,*}$ the z-component of the angular momentum and $v_c(r)$ its circular velocity. Following Genel et al. (2015), we define disc particles as the ones with $\eta > 0.7$. The rest are tagged as bulge-like (*hot component*). We highlight that further refinements of this disc-bulge kinematic distinction could be done (see, Scannapieco et al. 2009; Marinacci et al. 2014; Du et al. 2019, Zana et al. submitted), however, this level of refinement goes beyond the scope of this paper. Finally, the disc component is placed edge-on and we fit its surface density as:

$$\Sigma_{\text{d}}(z) = \frac{\Sigma_{z_0}^{\text{d}}}{2z_{\text{d}}} \text{sech}^2 \left(\frac{z}{z_{\text{d}}} \right) \quad (8)$$

where $\Sigma_{z_0}^{\text{d}}$ and z_{d} are the central surface density and vertical scale length of the disc.

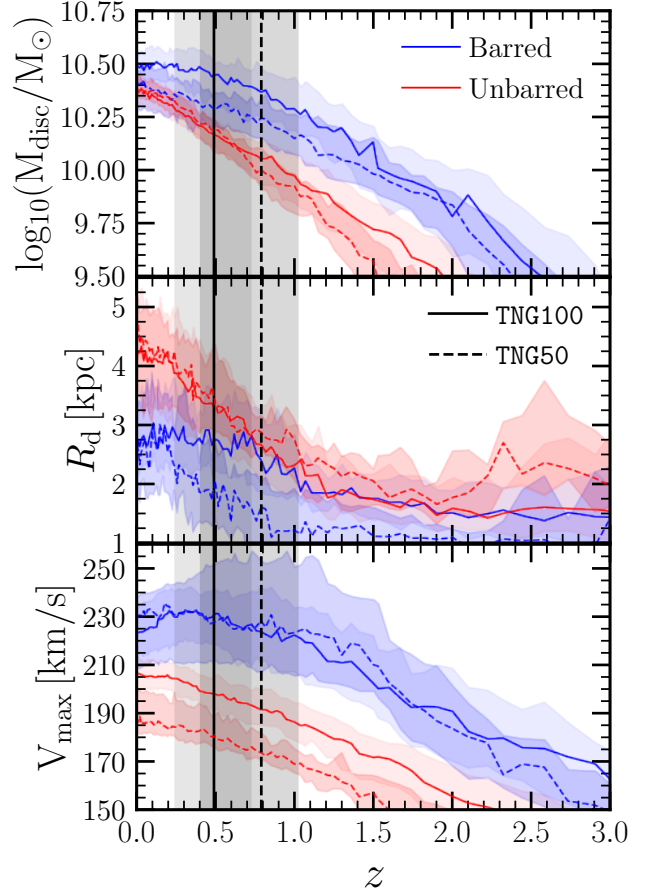


Figure 3. Redshift evolution of the stellar disc (M_{disc}), stellar scale length radius (R_{d}) and maximum circular velocity (V_{max}) for our $z=0$ barred (blue) and unbarred (red) sample. While solid (dashed) lines display the median value for TNG100 (TNG50), the shaded areas give the 32th – 68th percentiles. The solid (dashed) vertical line highlights the median redshift of the bar formation in TNG100 (TNG50) and the shaded grey area its 32th – 68th percentile.

3 THE GENERAL PROPERTIES OF BARRED AND UNBARRED GALAXIES

We start by analyzing the general properties of the barred and unbarred populations of galaxies in TNG100 and TNG50. In Fig. 3 we present the evolution of the three quantities relevant in the ELN-criterion: the stellar mass of the disc, M_{disc} , the disc scale length, R_{d} and the maximum circular velocity of the system⁵, V_{max} (see Eq.1). By construction, barred and unbarred galaxies have similar disc masses at $z=0$ ($M_{\text{disc}} \sim 10^{10.5} M_{\odot}$). However, barred galaxies assembled earlier and, at higher redshifts they display more massive discs. For instance, at $z \sim 1$ the discs of barred galaxies are ~ 0.5 dex more massive than of unbarred galaxies, with similar values obtained in both the TNG100 and TNG50. Regarding R_{d} , we can see the barred sample displays smaller values than the unbarred one: the discs of barred galaxies are more compact, likely because of their earlier formation time and their smaller DM halo spin, as we will discuss below and in Section 4.1. While being consistent in the overall behaviour, in this case we see some differences between

⁵ The rotation curve of the system is computed considering all the components, namely stellar, dark matter and gas.

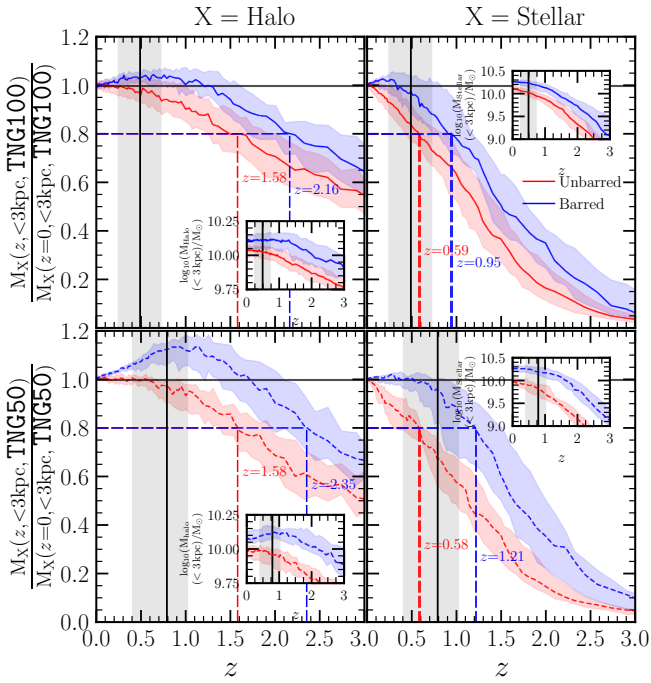


Figure 4. Assembly of the stellar and halo component of barred (blue) and unbarred galaxies (red) within a physical distance of 3 kpc. The inner plots display the total stellar and halo mass within a physical distance of 3 kpc. In all the panels shaded areas represent the 32th–68th percentile. The vertical black line represents the median formation time of the bar structure of the whole barred galaxy sample. The grey area is the 32th–68th percentile of the bar formation distribution. Whereas the upper panels display the results for TNG100, the lower ones show the same for TNG50. In all the panels the horizontal lines mark the instants at which the DM halo/stellar component reached 80% of their final values.

TNG100 and TNG50: in the TNG100 the barred and unbarred samples have similar values of R_d at high redshift ($z \gtrsim 1$) and start diverging at lower times. We emphasize that R_d of both samples starts to differ at the bar formation time. Therefore, it is not clear whether this is a cause or a consequence of the bar formation. On the other hand, for the case of TNG50, barred and unbarred galaxies always show a constant offset of ~ 1 kpc. Finally, differences are also seen in the maximum circular velocity. Regardless of redshift, barred galaxies are hosted in systems with $\sim 20\%$ larger V_{\max} in the TNG100, while differences can be as large as $\sim 40\%$ for the TNG50.

Before investigating how these values translate in to the ability of the ELN-criterion to capture the stability of the disc, we further investigate the general properties of the two populations. In Fig. 4 we present the assembly of the inner region (< 3 kpc) of the halo and stellar components. We highlight that the same trends are seen at $2 \text{ kpc} < r < 5 \text{ kpc}$ ⁶. Regarding the halo component (left panels), at $z=0$ the two samples display similar final masses, with differences smaller than 0.1 dex (see the inset). However, the redshift evolution is considerably different: the inner region

⁶ To explore possible dependencies with the halo and stellar mass, we have compared the build-up of a sample of bars and unbarred galaxies matched with the same DM halo mass and stellar mass at $z=0$. The comparison showed that, regardless of mass, barred galaxies assembled their stellar and DM components earlier.

of the halos of barred galaxies is significantly more massive at all redshifts. These differences in mass are reflected in the halo assembly, being faster for the barred sample. For instance, while the halos hosting barred galaxies aggregated 80% of their mass within 3 kpc by $z \sim 2$, those of unbarred galaxies did it by $z \sim 1.6$. Interestingly, the central halo component of both barred samples decreases at $z < 1.5$, with this effect being more pronounced in the TNG50 sample. Such depletion of dark matter in the central region can be due to the assembly of the stellar disc component. Indeed, [Yurin & Springel \(2015\)](#) reported that the presence of discs can reduce the DM halo in the inner parts of the galaxy by a factor of 2. The authors attributed this depletion to the gravitational shocks that DM particles experience as they pass through the disc. Interestingly, this decrease takes place around the bar formation time, indicating that bar structures might be also contributing to a redistribution of the dark matter component. Similar results were found by [Algorry et al. \(2017\)](#) when exploring the evolution of barred galaxies in the EAGLE simulation. Besides, these authors found that the DM redistribution correlates with the strength of the bar, being larger for the strongest ones. To check if this effect can explain the larger drop seen in the TNG50, in Fig. 2 we compared the values of A_2^{\max} in TNG100 and TNG50. Interestingly, we find that the median value of TNG50 is $A_2^{\max} \sim 0.4$ whereas in TNG100 it is $A_2^{\max} \sim 0.35$. While we can not exclude the fact that resolution effects can affect the A_2^{\max} values (see e.g. [Frankel et al. 2022](#)), these results support the correlation between the bar strength and the efficacy of dark matter depletion seen in [Algorry et al. \(2017\)](#).

The stellar component follows a similar behavior to that of dark matter: barred galaxies have a larger mass content and faster assembly in the inner region with respect to unbarred galaxies. The early build up of galaxies that eventually develop a bar component was also reported by [Rosas-Guevara et al. \(2020\)](#), who related it with the fact that barred galaxies experienced earlier and more efficient star formation episodes than unbarred ones. Indeed, when we look at the gas fraction⁷ (top panel of Fig. 5) we see that, regardless of redshift and radius, the barred sample exhausts the nuclear gas reservoir earlier than the unbarred one. Indeed, the recent observational study of [Fraser-McKelvie et al. \(2020\)](#) supports this scenario. The authors showed that, regardless of mass, star formation histories of barred galaxies peak at earlier times than their unbarred counterparts, suggesting that the bar hosts build up their stellar component at higher redshifts. Interestingly, when comparing the TNG100 and TNG50 barred galaxies, we can see that the latter consumed their gas reservoir faster. This could explain why bar structures were born earlier in TNG50 ($z \sim 0.7$) than in TNG100 ($z \sim 0.5$, see Fig. 2): faster gas consumption can lead to a faster disc assembly which, in turn, can induce bar instability leading to an earlier formation of a bar structure. On top of this, the faster gas consumption seen in TNG50 could shed light on why the bar structures formed in that simulation are stronger than their counterparts in TNG100. By performing several simulations with different gas fractions, [Athanasoula et al. \(2013\)](#) reported that bars in gas-poor galaxies were longer and reached a higher strength than the ones hosted in gas-rich galaxies.

To explore the relative assembly between the dark matter halo and the stellar component, in the lower panel of the left column of Fig. 5 we present the redshift evolution of the ratio between

⁷ We define the galaxy gas fraction as $f_{\text{gas}}(< r) = M_{\text{gas}}(< r) / (M_{\text{gas}}(< r) + M_{\text{stellar}}(< r))$

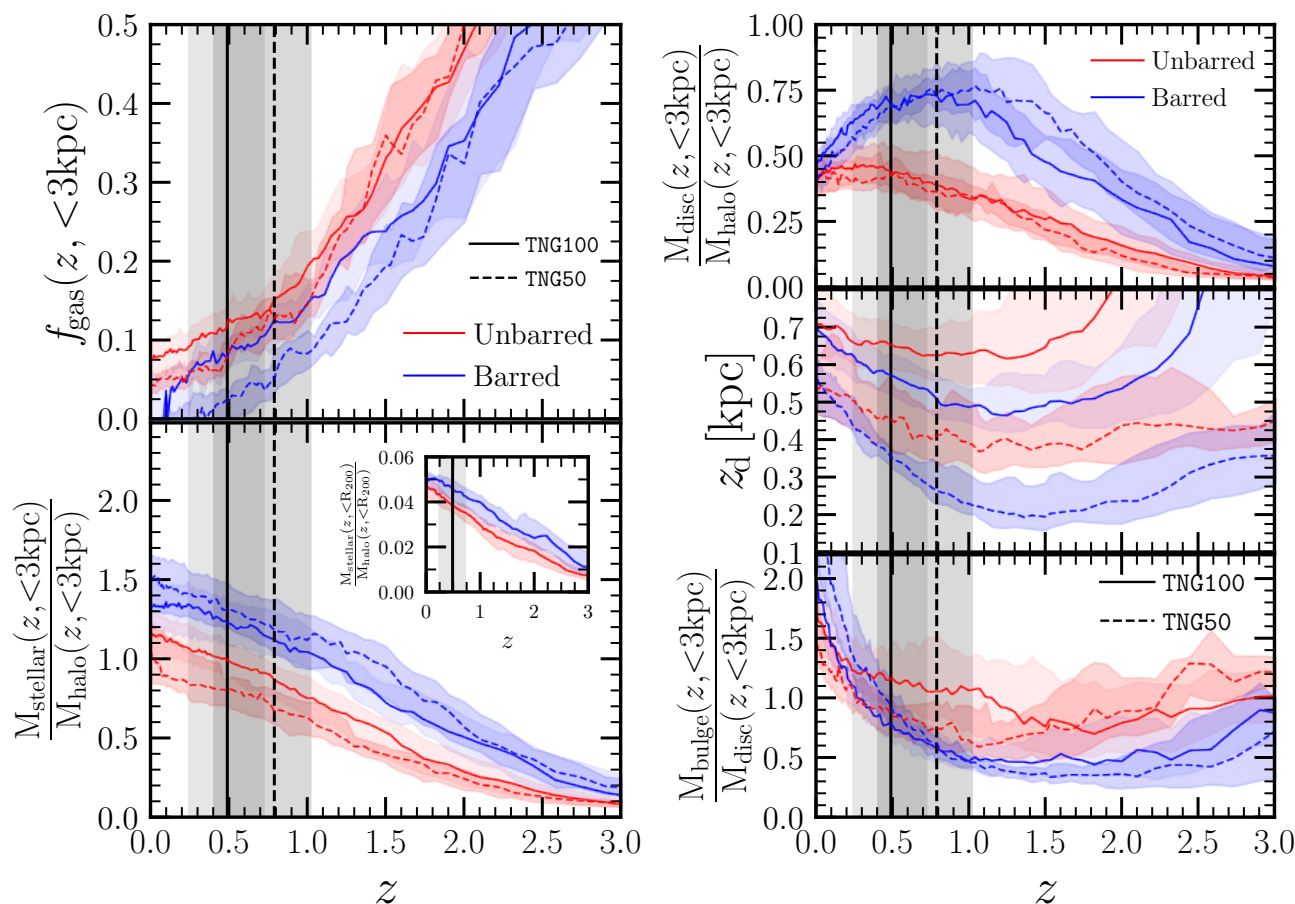


Figure 5. Left panels: Gas fraction, f_{gas} , and stellar-to-halo ratio at $<3\text{kpc}$. The inset displays the median value of the ratio between stellar and DM mass within the dark matter virial radius, R_{200} . **Right panels:** Disc-to-halo and bulge-to-disc ratio within $<3\text{kpc}$ and the vertical scale length of the disc (z_d). In all the plots, blue and red lines represent the median results for barred and unbarred galaxies whereas shaded areas are the 32th–68th percentile of the distribution. Solid and dashed lines represent the predictions for TNG100 and TNG50. The vertical solid and dashed black lines represent, respectively, the median formation time of the bar structure of the whole TNG100 and TNG50 barred galaxy samples. Grey area shows the 32th–68th percentile of the bar formation distribution.

the stellar and the halo mass (hereafter stellar-to-halo) for bars and unbarred galaxies at $<3\text{kpc}$. As we can see, regardless of redshift, the stellar-to-halo content is always larger for the barred sample (typically a factor >1.2) in both simulations. The difference is already present before bar formation and it persists down to $z = 0$. Such differences are still seen when we examine the total stellar-to-halo ratio within the halo virial radius (inset plot of Fig. 5). Similar trends were already reported by observational and theoretical works. On the observational side, [Cervantes Sodi \(2017\)](#), by analyzing galaxies in the SDSS-DR7, found an increasing trend of the bar fraction with larger stellar-to-halo mass ratios (see also [Cervantes Sodi et al. 2015](#)). Similar results were shown by [Díaz-García et al. \(2016\)](#) using the S⁴G survey ([Sheth et al. 2010](#)). On the theoretical side, [Valenzuela & Klypin \(2003\)](#) studied the transfer of angular momentum between halos and bars using N-body simulations of isolated disc galaxies. Interestingly, the authors found that the transfer of angular momentum from the bar to the outer regions of the disc leads to an increase (decrease) of the stellar (halo) mass content in the centre of the galaxy. On the same line we find the work of [Fragkoudi et al. \(2021\)](#) in which the authors, by analyzing the zoom-in AURIGA simulations, found that the hosts of barred galaxies display higher stellar-to-dark matter ratios than what is expected from the abundance matching relation. Finally, similar trends were found by [Rosas-Guevara et al. \(2021\)](#)

who reported that at fix stellar (or DM) mass, TNG50 barred galaxies were systematically more stellar dominated than the unbarred population.

Finally, we take a closer look at the evolution of disc and bulge components⁸ in the right panel of Fig. 5. We first show the evolution of the disc-to-halo ratio in the central region ($<3\text{kpc}$), seeing that barred galaxies display systematically larger values than unbarred ones, except for $z = 0$. Before bar formation, the disc-to-halo ratio of barred galaxies rises steeply. These results support the results of [Mayer & Wadsley \(2004\)](#) and [DeBuhr et al. \(2012\)](#), who found through numerical simulations of isolated galaxies that the disc-to-halo mass ratios within the typical disc radius can be a fundamental factor for determining the development of barred structures in disc-dominated galaxies. However, after bar formation ($z < 0.5$ for TNG100 and $z < 0.7$ for TNG50), the disc-to-halo ratio of barred galaxies drops. This effect can be caused by a combination of factors. One could be that the bar structure triggers a buckling of the stellar orbits, leading to the formation of a pseudobulge component ([Pfenniger & Norman 1990](#); [Bureau & Freeman 1999](#); [Combes](#)

⁸ The division between disc and bulge-like particles has been done as explained in Section 2.2.1

2009; Kormendy & Ho 2013; Fragkoudi et al. 2017). Another alternative could be that the bar structure itself is dominated by more radial orbits, which are likely to appear in a mildly rotating component rather than in a cold disc (i.e., $\eta > 0.7$). This would cause our morphological decomposition to classify some of the stellar particles of the bar as a bulge (*hot*) component. Besides the different behaviour in the disc-to-halo ratio, the discs of barred and unbarred galaxies are distributed differently also in the vertical axis (z_d). As shown, barred galaxies display colder discs than unbarred ones, with vertical heights up to 1.5 times smaller. We stress that TNG50 displays smaller values of z_d than TNG100, principally as a result of resolution effects. As shown by Pillepich et al. (2019) (see their Figure B.2), lower resolution simulations have puffier stellar discs. Despite the differences between TNG100 and TNG50, our results agree with the theoretical work of Athanassoula & Sellwood (1986) and Athanassoula (2003) which reported that dynamically hot discs can delay or even suppress the formation of bars as a consequence of large random motions hindering the growth of bar modes. Observational evidence of such an effect can be found in Sheth et al. (2012): analyzing massive galaxies at $z < 0.8$ the authors found that bar structures are preferentially in galaxies with massive and dynamically cold discs.

Lastly, concerning the evolution of the bulge-to-disc ratio, we see that at $z \gtrsim 0.5 - 0.7$ unbarred galaxies display values larger than 0.5, pointing out that the bulge component dominated the inner parts of the galaxy. In contrast, barred galaxies have bulge-to-disc ratios smaller than 0.5, with the disc governing the inner galaxy. At $z \lesssim 0.5 - 0.7$, whereas no dramatic change is seen in the unbarred sample, barred galaxies underwent a change of trend. Specifically, the bulge gains more relevance as bar formation triggers the development of a bulge-like component (i.e., a structure with a *hotter* kinematics than the disc). Finally, we highlight that the decreasing trend seen in both samples at $z \gtrsim 1.5$ is likely caused by the fact that galaxies start with an irregular morphology, causing our morphology distinction to classify most of the stellar particles as bulge-like (or hot component). Later on, as the galaxy evolves, it develops a well-defined disc component and creates a bulge structure through secular and merger processes. We refer the reader to Zana et al. (submitted) for further details about the assembly of discs and bulges in TNG simulations.

Before moving on to the direct test of the ELN-criterion for detecting the capability of a galaxy to form a bar, we conclude from this first analysis that the bar properties and their host galaxies in the TNG50 and TNG100 simulations generally confirm several trends derived in earlier works: galaxies that eventually develop a bar assemble at earlier times, are characterized by larger stellar-to-halo ratios in the inner regions and their discs are more massive, but smaller and colder, with respect to unbarred galaxies. Early global assembly and a fast build up and compactness of the disc seem to be key to bar formation. Moreover, we also find indications that the bar is able to redistribute the dark matter component in the inner parts of the galaxy, in particular diminishing its concentration.

4 ACCURACY OF THE ELN-CRITERION

After exploring the global differences between bars and unbarred galaxies and determining the evolution of the quantities employed by the ELN-criterion, we now examine its ability to determine whether a bar actually forms. To do this, we do not evaluate the criterion only

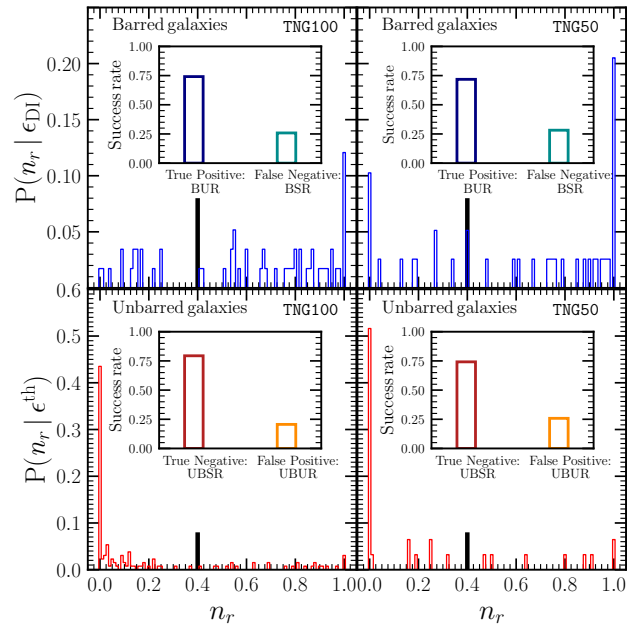


Figure 6. Distribution of n_r for all the barred (top) and unbarred (bottom) galaxies. Left and right panels represent the predictions for TNG100 and TNG50, respectively. The solid black vertical line highlights the threshold $n_r = 0.4$, which we use to determine the success rate of the ELN-criterion, assuming a threshold of $\epsilon = 1.1$. The derived success rate is shown in the inset. True positives, i.e. barred galaxies correctly identified by the criterion, are labelled BUR (bar in the unstable region). On the other hand, false negatives, i.e. barred galaxies in which the criterion does not find bar instability, are labelled BSR (bars in the stable region). Similarly, unbarred galaxies properly identified by the criterion (true negative) are called UBSR (unbarred in the stable region) and unbarred galaxies wrongly considered unstable are called UBUR (unbarred in the unstable region).

at the snapshot corresponding to bar formation, but over a broader time interval. We define a new variable, n_r , which measures the fraction of time spent by the galaxy in the bar unstable region. Specifically, it is defined as:

$$n_r = \frac{1}{t_f^{\text{bar}}} \sum_{i=\text{snp}(z_f^{\text{bar}})}^{\text{snp}(z=0)} \Delta t(i, i+1 | \epsilon \leq \epsilon^{\text{th}}), \quad (9)$$

where $\Delta t(i, i+1 | \epsilon \leq \epsilon^{\text{th}})$ corresponds to the time interval between the snapshot i and subsequent one, $i+1$, in which the galaxy ϵ value is smaller than $\epsilon^{\text{th}} = 1.1$ (see Eq. 1). The index i runs from the snapshot of the bar formation until the last simulation snapshot (i.e. $z=0$). Therefore, $n_r=0$ for galaxies that never satisfy the condition of $\epsilon \leq 1.1$ at a snapshot after bar formation ($\text{snp} \geq \text{snp}_f^{\text{bar}}$). On the contrary, $n_r=1$ for galaxies that always satisfy the instability criterion. In the top panels of Fig. 6 we show the distribution of n_r for barred galaxies in TNG100 (left) and TNG50 (right). Most barred galaxies have a large value of n_r , with a clear maximum at $n_r \sim 1$ (more pronounced in TNG50), showing that the majority of barred galaxies satisfy the ELN-criterion for a significant fraction of time after bar formation. However, there is a small number of barred galaxies with low values of n_r , pointing out that some barred galaxies do not satisfy $\epsilon \leq 1.1$ for most of the snapshots after bar formation. On the other hand, in the lower panel of Fig. 6 we present the n_r distribution for unbarred galaxies. For this sample, we have decided to use as $\text{snp}(z_f^{\text{bar}})$ the median $\text{snp}(z_f^{\text{bar}})$ of the

barred galaxies (see discussion of Section 2.2). The vast majority of unbarred galaxies are characterized by low values of n_r , indicating that the ELN-criterion is generally able to capture the stability of disc galaxies.

Based on the distributions shown in Fig. 6 we have chosen a threshold of n_r (n_r^{th}) equal to 0.4 to define the cases we consider that the ELN-criterion successfully identifies disc stability. The value for this threshold is arbitrary, and we have checked that the results do not significantly change when varying n_r^{th} between 0.3–0.5. In the inset plots of Fig. 6 we present the derived success rate of the ELN-criterion. For barred galaxies, we obtain a success rate of $\sim 74/72\%$ with a failure fraction of $\sim 26/28\%$ for the TNG100/TNG50, respectively. From hereafter, galaxies in the former case are going to be called *bars in the unstable region* (BUR, true positive) while the ones in the latter are going to be tagged as *bars in the stable region* (BSR, false negative). Regarding the unbarred sample, the number of galaxies correctly identified as unbarred by the ELN-criterion are $\sim 79/75\%$, while $\sim 21/25\%$ are misclassified as being unstable, for TNG100 and TNG50, respectively. In analogy with the barred sample, from now on we refer to the unbarred galaxies correctly classified as *unbarred in the stable region* (UBSR, true negative) while the ones misclassified are going to be tagged as *unbarred in the unstable region* (UBUR, false positive).

To explore the robustness of the choice of 1.1 as threshold value in the ELN-criterion, we also calculated the success rate varying the adopted threshold. As expected, the number of correctly identified bars increases when adopting a larger threshold, at the expense of a larger number of unbarred galaxies being tagged as unstable. For example, if we adopt $\epsilon^{\text{th}} = 1.2$, a value also used in the literature (Lagos et al. 2018; Izquierdo-Villalba et al. 2019), the number of barred galaxies correctly identified increases up to $\sim 85/77\%$ for TNG100/TNG50, while the number of correctly identified unbarred galaxies drops to $\sim 67/55\%$ for TNG100/TNG50. We find that the best balance between correctly identified barred and unbarred galaxies is reached when adopting the threshold of 1.1 as originally proposed by Efstathiou et al. (1982) (see also Yurin & Springel 2015). We have also explored how the success rate of the ELN-criterion changes depending on the adopted time of bar formation i.e., $\text{snp}(z_f^{\text{bar}})$. We have found that moving to any other snapshot within $t_f^{\text{bar}} \pm 40t_{\text{dyn}}$ (where t_{dyn} the disc dynamical time at bar formation time), the success rate for barred and unbarred galaxies does not change. Finally, we have explored the success rate when the summation of Eq. 9 is performed only in a few snapshots around the bar formation, specifically over the snapshots within $10t_{\text{dyn}}$ before and $40t_{\text{dyn}}$ after the bar formation time. Again, we find only minor differences with the success rates obtained above.

In the upper panels of Fig. 7 we present, for both TNG100 and TNG50, the median evolution of A_2^{max} and ϵ as a function of δt (see Eq. 5) for the BUR and BSR samples (true positive and false negative, respectively). As we can see, the first sample displays a good correlation between ϵ and the bar strength evolution, i.e., ϵ decreases down to values smaller than 1.1 when A_2^{max} increases above the threshold value of 0.2 after the time of bar formation ($\delta t \sim 0$). On the other hand, the galaxies belonging to the BSR sample are characterized by ϵ values systematically larger than 1.1 before and after bar formation. We note here that the BUR sample has a median bar formation time ($z \sim 0.5/0.8$ for TNG100/ TNG50) larger than the one of the BSR sample ($z \sim 0.25/0.35$ for TNG100/ TNG50). On top of this, the evolution of the A_2^{max} median value is

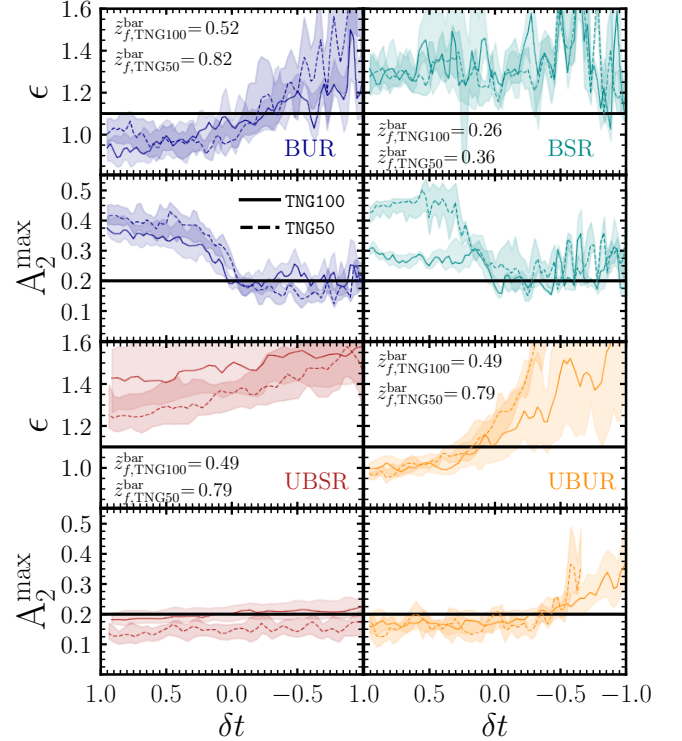


Figure 7. Upper panels: Dark blue thick lines represent the evolution of the median values of ϵ and A_2^{max} for the *barred in the unstable region* sample (BUR - true positives). Cyan lines represent the same but for the *barred in the stable region* (BSR - false negatives). Shaded areas display the percentile 32th–68th. In each panel we show the z_f^{bar} , i.e., the median formation redshift for each sample. **Lower panels:** The same as the upper panels but for the *unbarred in the stable region* sample (red, UBSR - true negative) and *unbarred in the unstable region* sample (orange, UBUR - false positive). In all the plots, solid and dashed lines represent the results for TNG100 and TNG50, respectively. For unbarred galaxies, times are normalized using the median formation time of the whole barred sample of the corresponding simulation.

different for the BSR and the BUR galaxies. While TNG100 predicts that the BUR sample displays systematically larger A_2^{max} values than BSR, TNG50 predicts the opposite. These differences could hint at the fact that the barred galaxies of the BSR sample might have a different evolution than the one of the BUR sample and/or their bars form via different processes. In the bottom panels of the same figure, we show the median evolution of A_2^{max} and ϵ as a function of δt for the unbarred sample divided into UBSR (true negative) and UBUR (false positive) samples. As mentioned before, for unbarred galaxies δt has been computed using the median formation time of all barred galaxies. As we can see, the UBSR galaxies are characterized by values of ϵ above the threshold value of the ELN-criterion and a flat A_2^{max} evolution with time, confirming the stability of the sample. For the UBUR sample, instead, we find a similar evolution for A_2^{max} , but ϵ decreases with time, reaching values below the disc stability threshold. We note that in some cases, in particular at early times, A_2^{max} can be larger than 0.2. Those fluctuations in A_2^{max} are not related to a bar structure given that the phase ϕ associated with that A_2^{max} within the bar length is not constant. Instead, large values of A_2^{max} can be caused by any non-axisymmetric structure such as spiral arms or interactions with small satellites.

Based on the analysis performed in this section, we can conclude

that, despite its simplicity, the ELN-criterion is able to correctly identify the formation or absence of a barred structure in the majority of the cases. This is in agreement with the results of [Yurin & Springel \(2015\)](#) who found a correlation between the outcome of the ELN-criterion and the $z=0$ bar strength by analyzing simulations of Milky-Way type galaxies. However, the recent work by [Algorry et al. \(2017\)](#) (EAGLE simulation) and [Marioni et al. \(2022\)](#) (zoom-in simulations) pointed towards the opposite direction, suggesting that ELN-criterion is an incomplete indicator of disc instability. The main difference between our analysis and the one performed in these works consists in that they check the ELN-criterion just at the bar formation time, defined as the moment in which the galaxy fulfils $A_2^{\max} > 0.2$. Probably, averaging the ELN-criterion over several snapshots (as we do) might also improve the robustness of the criterion in their simulations. Instead of being an instantaneous process, the development of a bar structure can take several galaxy dynamical times. On the observational side, the recent paper of [Romeo et al. \(2022\)](#) explored the capability of ELN-criterion to detect the presence of bar structures in a sample of 91 disc dominated galaxies with $10^{6.5} - 10^{11.5} M_{\odot}$. The authors found that ELN-criterion was only successful in 55% of the cases. Even though these results differ from our findings, a direct comparison between their work and our results is not straightforward given the different ranges of mass probed by our analyses and our pre-selection of strong barred galaxies. Trough private communication with the authors, we checked that in the same mass range probed by this work the results of [Romeo et al. \(2022\)](#) showed that the large majority of barred galaxies reside in the bar-unstable region, in agreement with our results. However, non-barred galaxies tend to be far from stability according to the ELN-criterion.

Despite the overall success, the stability/instability of almost one quarter of the galaxies is not correctly captured by the ELN-criterion. In what follows, we study the differences in the properties of the BUR and UBUR samples and the BSR and UBSR samples, with the goal of identifying the reasons why the ELN-criterion fails in certain instances.

4.1 The stellar and dark matter component of stable and unstable galaxies

We start by looking at the redshift evolution of the physical quantities used in the ELN-criterion, M_{disc} , R_{d} and V_{max} , as in Fig. 3, but now separately for the BUR/BSR (barred) and UBUR/UBSR (unbarred) populations. We show this in Fig. 8. Regarding the barred sample (left column), in TNG100 BUR galaxies (true positive) have generally more massive discs and larger V_{max} than the BSR ones (false negative). However, these trends disappear in TNG50 where both samples display comparable M_{disc} and the BSR sample reaches large median V_{max} . Despite these small differences, TNG100 and TNG50 agree that BUR galaxies have more compact discs, with differences of up to 1 kpc with respect to BSR at $z_{\text{f}}^{\text{bar}}$. The difference in the scale length of the disc is what primarily drives the different evolution of the ϵ parameter in the two samples. While V_{max} and M_{disc} show relatively small variations between BUR/BSR and UBUR/UBSR ($\sim 10 - 20\%$), R_{d} can nearly double its value, which implies a change in ϵ by a factor up to 1.4. Concerning the unbarred samples (right column of Fig. 8), UBSR (true negative) and UBUR (false positive) present similar redshift evolution in M_{disc} and V_{max} , but they show significant differences for R_{d} at $z < 1$. While the scale lengths of UBUR galaxies experience a very mild evolution ($R_{\text{d}} \sim 2.5$ kpc) those of UBSR increase rapidly, reaching by $z \sim 0$

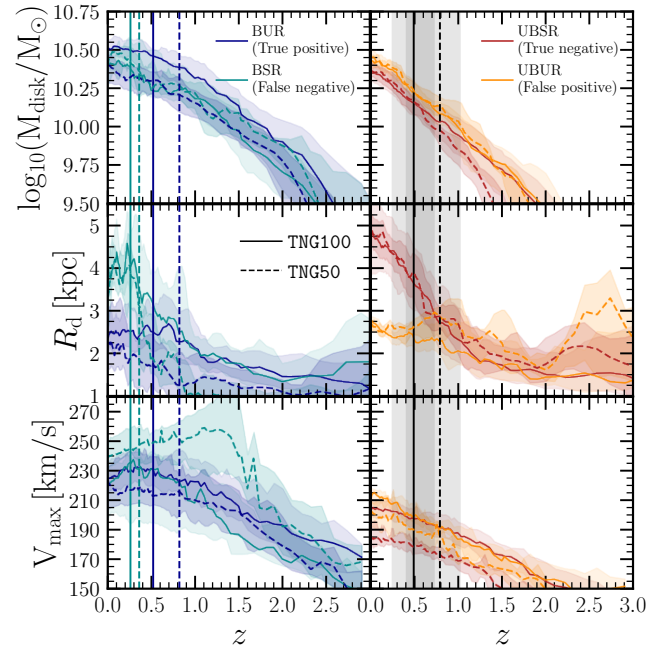


Figure 8. Evolution of the stellar disc (M_{disc}), stellar scale length radius (R_{d}) and maximum circular velocity (V_{max}) for the BUR (dark blue), BSR (cyan), UBUR (orange) and UBSR (red) sample. Solid and dashed lines represent the results for TNG100 and TNG50, respectively. While lines display the median value, the shaded areas display the 32th – 68th percentiles. For barred galaxies, the solid vertical lines highlight the median redshift of bar formation for each barred sample (we do not add the percentiles to avoid overcrowding). For unbarred galaxies, the solid vertical line highlights the median redshift of bar formation of all barred galaxies.

values of $R_{\text{d}} \sim 4.5$ kpc. These trends are found in both TNG100 and TNG50. As for the barred sample, the difference in the scale length of the disc is what causes the different evolution of the ϵ parameter for UBSR and UBUR. UBUR galaxies are very compact and have low values of ϵ , thus, according to the ELN-criterion, they should be prone to instabilities. Comparing the BUR (true positive) and the UBUR (false positive) sample (i.e. the two galaxy samples with the smallest radii), we see that the principal difference is seen for disc mass assembly, which happens earlier in the barred sample. We calculated the average formation time of the DM and stellar component of the two samples, and we found that the DM halos (stellar component) of BUR galaxies aggregated 80% of their $z=0$ mass at < 3 kpc by $z \sim 2$ ($z \sim 1$) whereas UBUR ones did it ~ 1.5 Gyr later ($z \sim 1.5$ and $z \sim 0.5$ for the DM and stellar component, respectively). To summarize, Fig. 8 points out that R_{d} is the main property that leads to failures of the ELN-criterion. Large values of R_{d} are what cause some barred galaxies to be misclassified as unbarred, and, conversely, the misclassified unbarred galaxies have untypically small values of the scale length.

To explore the origin of the differences in R_{d} in the samples of barred and unbarred galaxies, in the right panel of Fig. 9 we look at the modulus of the DM halo spin, $|\vec{\lambda}_{\text{h}}|$, computed following [Bullock et al. \(2001\)](#):

$$\vec{\lambda}_{\text{h}} = \frac{1}{\sqrt{2}} \frac{\sum_j M_j \vec{r}_j \times \vec{v}_j}{M_{200} V_{200} R_{200}} \quad (10)$$

where M_j , \vec{r}_j and \vec{v}_j are the mass, radius and velocity of the j -th

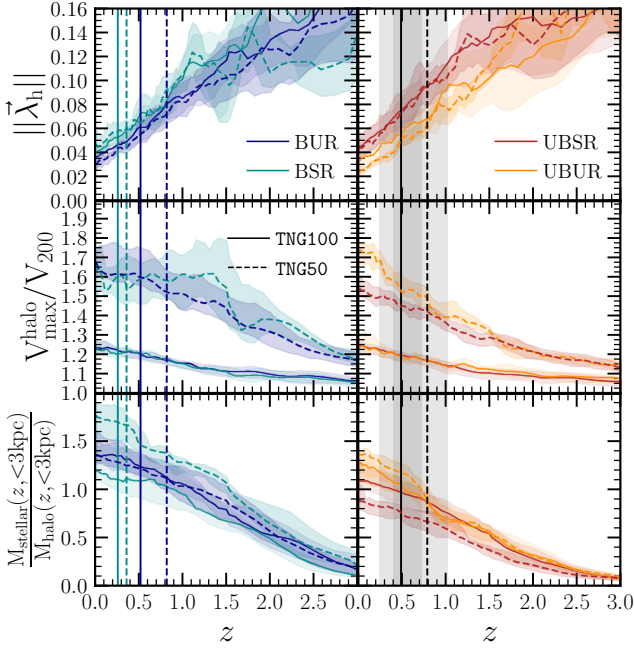


Figure 9. Evolution of the DM halo spin modulus ($|\vec{\lambda}_h|$), halo concentration ($V_{\text{max}}^{\text{halo}}/V_{200}$) and ratio between stellar and halo mass at $<3\text{kpc}$. The color coding, line styles and vertical lines are the same as for Fig. 8.

dark matter particle. M_{200} , V_{200} and R_{200} correspond to the virial mass, velocity and radius of the subhalo, respectively. The samples with the largest R_d , i.e. UBSR and BSR (true and false positive, respectively), are the ones with the highest $|\vec{\lambda}_h|$ parameter and no significant differences are seen between TNG100 and TNG50. We highlight that these trends are important at low redshift ($z < 1$) given that at high redshift the scatter dominates and the distributions of the four samples do not differ significantly. These results are in agreement with Mo et al. (1998a) which reported that exponential discs embedded inside Navarro-Frenk-White DM halos display scale lengths which scales proportionally to $|\vec{\lambda}_h|$ (see Eq.10 of Mo et al. 1998a). Therefore, the different R_d evolution between BUR/BSR and UBUR/UBSR seems to be the outcome of the different spinning DM halo in which these samples are hosted. Such correlation between galactic sizes and $|\vec{\lambda}_h|$ has been debated during in the recent years. For instance, Jiang et al. (2019), by using different zoom-in simulations of central and massive galaxies (larger or equal than Milky-Way type galaxies) found that the halo spin is not an useful predictor of the galaxy size, rather the halo virial radius is the property which displays the better correlation. This lack of correlation was also reported by Scannapieco et al. (2009) in a suit of eight isolated galaxies embedded inside Milky Way type halos. On the other hand, Yang et al. (2021) analyzed EAGLE and TNG100 simulations and found that galactic sizes strongly correlate with the spin parameters of their dark matter halos (see the similar conclusion of Grand et al. 2017).

We also note that unbarred galaxies (UBSR or true negative represents $\sim 80\%$ of the unbarred sample) typically have larger spin values than barred ones. The role of halo spin in the formation and growth of bars has so far been rather controversial. Using a suite of isolated simulations of discs embedded in dark matter halos with various spin properties, Saha & Naab (2013) showed

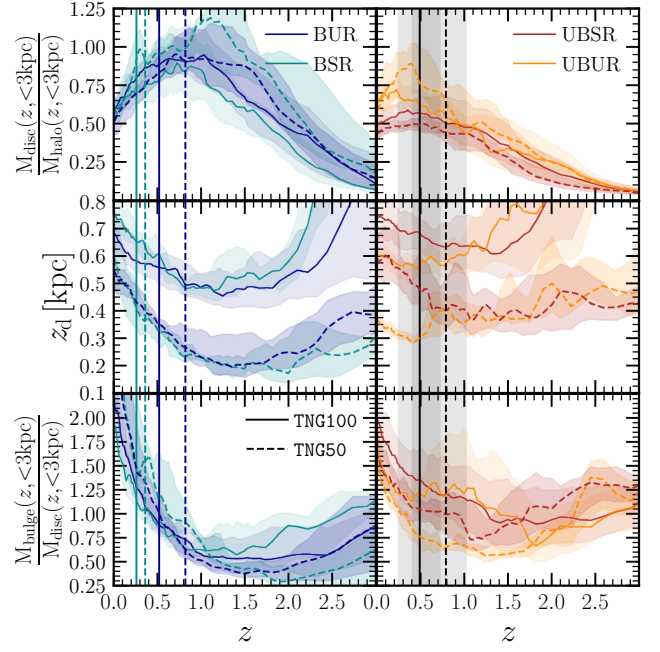


Figure 10. Evolution of the median values of the disc-to-halo ($r < 3\text{kpc}$), vertical scale length of the disc (z_d) and the bulge-to-disc ($r < 3\text{kpc}$). The color coding, line styles and vertical lines are the same as for Fig. 8.

that the larger the spin of co-rotating halos, the faster, the stronger and the longer is the bar that the simulated galaxy is capable of developing. On the other hand, Long et al. (2014), also using a set of isolated galaxy simulations, found that spinning dark matter halos ($|\vec{\lambda}_h| > 0.03$) can heavily reduce the secular growth phase of stellar bars and decrease their pattern speed. The observational study of Cervantes-Sodi et al. (2013) points towards in a similar direction finding a decrease of the fraction of galaxies hosting strong bars towards large $|\vec{\lambda}_h|$. While it is beyond the scope of this work to study the connection between bar properties and halo spin, our results indicate that most bars (BUR or true positive represents the $\sim 75\%$ of the barred sample) are hosted by more slowly spinning halos, as also shown for the TNG50 in Rosas-Guevara et al. (2021).

In the middle panel of Fig. 9 we further investigate the dark matter halo properties, looking at the concentration. We compute it as the ratio $V_{\text{max}}^{\text{halo}}/V_{200}$, where $V_{\text{max}}^{\text{halo}}$ is the maximum rotational velocity of the halo component. This quantity is a proxy of the DM halo concentration and is widely used in many works (see e.g. Gao & White 2007), as it does not require any model to fit the simulation data. As shown, TNG50 predicts larger concentrations than TNG100. However, small differences are seen between BUR (true positive) and BSR (false negative), and between the UBSR (true negative) and UBUR (false positive) samples. In the TNG50 there is a weak indication that barred galaxies (BUR represents the $\sim 75\%$ of the barred sample) are hosted by more concentrated halos, as also discussed by Rosas-Guevara et al. (2021). Despite that, the results presented here seem to point out that DM concentration does not play an important role (if any) in the bar formation.

To explore the interplay between the DM and stellar components, in the lower panel of Fig. 9 we present the stellar-to-halo ratio within 3kpc . As shown in Fig. 5, barred galaxies have generally

larger stellar fractions than unbarred galaxies. Only for TNG100 the BSR galaxies display slightly smaller stellar-to-halo ratios than the BUR ones. For TNG50, instead, the stellar-to-halo ratio is larger for the BSR sample. Concerning the unbarred population, we can see that the UBUR and UBSR samples behave in a similar way at $z > 1$. However at lower redshifts, their trends diverge, and the UBUR galaxies have larger stellar-to-halo ratios.

In Fig. 10 we look at the properties of the disc component. In the top panel, we show the disc-to-halo ratio in the inner region. Both bar samples (BUR and BSR) are characterized by a dominant central disc component, which declines after bar formation as the galaxy develops a pseudobulge or our morphological decomposition classifies some bar particles as a bulge as a consequence of their radial orbits (see the discussion for Fig. 5). The UBUR sample has a more dominant disc with respect to the average unbarred population (UBSR), which contributes to the misclassification of these galaxies according to the ELN-criterion. Still, both unbarred samples have significantly lower disc-to-halo ratios at early times with respect to barred galaxies. Looking at the vertical extent of the disc, we also do not see significant differences between the BUR and BSR samples: all barred galaxies have generally colder discs with respect to unbarred galaxies, and TNG50 produces thinner discs. However, the misclassified unbarred galaxies (UBUR) have thinner discs than the average unbarred population, with values closer to the ones of barred galaxies. Despite this, UBUR galaxies have z_d values ~ 2 times larger than the ones displayed by BUR and BSR samples. We highlight that the trends at $z \gtrsim 1.5$ should be considered with caution since the galaxy morphology is irregular and the resolution of the simulation might have an impact on our results.

Finally, in the lower panel of Fig. 10 we explore the evolution of the bulge-to-disc ratio of our sub-samples of barred and unbarred galaxies. Before bar formation, the BSR sample (false negative) displays slightly larger ratios than the BUR one (true positive), but both barred samples have significantly less predominant bulges with respect to the unbarred sample. After bar formation, both BUR and BSR galaxies show a fast increase of the bulge component, caused by the development of a pseudobulge structure. The systematically larger B/D ratios of unbarred galaxies suggest that the bulge structure plays an important role in suppressing the development of bars (see, e.g., the early works of [Ostriker & Peebles 1973](#); [Toomre 1981](#); [Sellwood 1980](#); [Sellwood & Evans 2001](#)). Indeed, using the *Eris* and *ErisBH* zoom-in simulations of a Milky Way-type halo, [Bonoli et al. \(2016\)](#) found that early suppression of bulge formation (possibly due to AGN feedback), can lead to discs more prone to instabilities. More recently, using N-body simulations, [Kataria & Das \(2018\)](#) and [Kataria et al. \(2020\)](#) showed a delay in the bar formation as a function of the galaxy bulge-to-disc ratio (B/D). Particularly, they reported an upper limit of $B/D \sim 0.2 - 0.5$ above which the development of a bar is suppressed.

Based on the above analysis, we conclude that early disc assembly and the absence of a prominent bulge component are necessary conditions for the formation of a bar. Massive and compact discs without bars, wrongly classified by the ELN-criterion as unstable galaxies (UBUR or false positive) have indeed a prominent bulge and assembled at later times. When analyzing the details of the barred samples, the primary difference between the BUR (true positive) and BSR (false negative) galaxies is the average size of the disc, which seems to be linked to the halo spin. In what remains of the section we will further discuss the differences between these

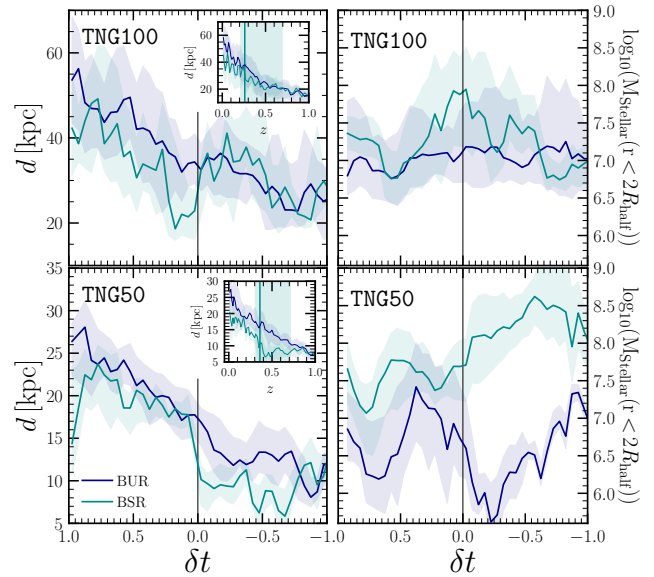


Figure 11. Distance (left) and stellar mass (right) of the closest neighbour for BUR (dark blue) and BSR (cyan) galaxies as a function of δt . The dark vertical line highlights $\delta t = 0$. The inset displays the same but as a function of redshift for the BUR and BSR samples. The horizontal blue line (shaded area) represents the median (32th – 68th percentile) bar formation time of BSR galaxies.

two populations, and speculate on the possibility of different trigger mechanisms for their bar structure.

4.2 The missed barred galaxies in the ELN-criterion: An external triggering?

As shown in Section 4, the BSR sample (false negative) is composed of barred galaxies for which the ELN-criterion is not able to predict disc instability. As extensively discussed in Section 4.1, both samples are characterized by early-assembling dominant discs, but the discs of BUR galaxies are significantly more compact, likely because of the lower spin parameter of their host dark matter halos.

These differences make us wonder whether the two barred populations (BUR and BSR) have a common origin, or if the instabilities in the two samples could be triggered by different processes. In the general picture of bar formation, which underlies the ELN-criterion, disc instabilities are a *secular process*, in which the slow growth of a self-gravitating stellar disc supported mainly by rotation leads to global dynamical instabilities which then trigger the formation of a bar ([Kalnajs 1972](#); [Athanasoula & Sellwood 1986](#); [Shen et al. 2003](#); [Moetazedian et al. 2017](#); [Yurin & Springel 2015](#); [Zana et al. 2018a](#)). However, a number of authors have argued that bar structures can form (or disappear) during galaxy interactions such as mergers or flybys (i.e., “external triggers”, [Miwa & Noguchi 1998](#); [Berentzen et al. 2004](#); [Łokas et al. 2014](#); [Peschken & Łokas 2019](#); [Ghosh et al. 2021](#)). The time resolution of the outputs of the TNG100 and TNG50 simulations is unfortunately not sufficient to perform a detailed analysis on the role of external triggers on bar formation. Such a study would require a re-running of specific regions of the simulation domain with higher output frequency, as done for instance in [Zana et al. \(2018a\)](#), and goes beyond the scope of this paper. In an attempt to assess the role of

external triggers in the formation of bars in our samples, in Fig. 11 (left panel) we present the distance to the closest neighbour as a function of time for the BUR and BSR galaxies. Interestingly, for both TNG100 and TNG50, the distance to the closest neighbour for BSR galaxies drops/experiences a fast rise at $-0.15 < \delta t < 0.15$, i.e. around the time of bar formation. In contrast, the distance for the BUR galaxies does not show such a clear feature, with a typical distance values $\sim 1.5-2$ times larger than for BSR. Besides the distance, the stellar mass of the closest neighbour is also different for BUR and BSR samples (right panel of Fig. 11): the neighbours of BSR galaxies are systematically more massive, especially at the bar formation time where the differences can reach up to 1 dex.

Even though this analysis can not conclusively ensure that BSR galaxies developed their bar as a consequence of a close interaction, it provides suggestive clues in that direction. Indeed, external triggering could explain why the ELN-criterion is not able to detect the disc instabilities for BSR galaxies. The work of Izquierdo-Villalba et al. (2019) used the L-Galaxies SAM to explore the possibility that the ELN-criterion could detect some disc instabilities caused by external triggering. Specifically, by following the history and the physical conditions of the galaxy in which a disc instability takes place, the authors distinguished between instabilities that are merger-induced and the ones that are a consequence of the slow, secular evolution of galaxies. Izquierdo-Villalba et al. (2019) showed that bar/pseudobulge structures in massive galaxies are generally a result of secular processes, although some massive discs can become bar unstable after a minor merger, which prompts the formation of a nuclear ellipsoidal component. In agreement with our findings (see Fig. 11) these authors reported that merger-induced disc instabilities are rare and occur mostly at $z \sim 1$ with a sharp cut-off towards higher redshifts. Despite their attempts to link the ELN-criterion with an external triggering mechanism, further analysis of this is needed. Indeed, the recent papers of Zana et al. (2018a,b) suggest that external perturbers could have a negative effect on the bar formation. By analyzing a state-of-the-art cosmological zoom-in simulations the authors found that minor mergers or close fly-by can delay the bar formation. Even more, they can have a destructive effect, weakening or destroying strong bars. Taking into account the results shown here and all the works presented in the literature, additional dependencies could be added in the ELN-criterion to determine if a close galaxy encounter or a merger has the capability of triggering/delaying the formation of a bar structure.

5 CONCLUSIONS

In this paper we explored, for the first time in a systematic way, the performance of the Efstathiou et al. (1982) analytic criterion (ELN-criterion) for disc instability using a sample of barred and unbarred galaxies extracted from large cosmological hydrodynamical simulations. Specifically, we made use of the catalogues of Rosas-Guevara et al. (2020) and Rosas-Guevara et al. (2021), composed of barred and unbarred disc galaxies (disc-to-total ratios > 0.5) extracted from the TNG100 and TNG50 simulations at $z=0$. To ensure high-enough resolution, we consider only disc galaxies with stellar masses larger than $10^{10.4} M_{\odot}$. Indeed, galaxies with such masses have proven to be the preferential hosts and birthplaces of bar structures in the low- z Universe (see e.g. Gadotti 2009; Cervantes Sodi et al. 2015; Gavazzi et al. 2015)

We first of all compared the physical properties of strongly barred and unbarred galaxies. By analyzing the disc component we found that the discs of the barred sample generally assembled earlier and the discs are more compact (~ 1 kpc of difference). The early assembly of the disc of barred galaxies is related to the early assembly of the dark matter and stellar components, and to early consumption of the available gas. On top of that, the distribution of the baryonic component is different for barred and unbarred galaxies: the central stellar-to-halo and disc-to-halo ratios are significantly larger for barred galaxies than for unbarred ones, in agreement with other theoretical work (Algorry et al. 2017; Fragkoudi et al. 2021). Regarding the bulge component, we found the opposite trend, with barred galaxies being characterized by a subdominant bulge before bar formation. Only after the development of the bar, the bulge component grows, likely because of bar buckling which leads to the formation of a pseudobulge and/or because our morphological decomposition classifies the stellar particles subsiding the bar structure as bulge-like (*hot component*).

The differences mentioned above clearly indicate that disc galaxies that develop a prominent bar structure have generally a very different history than disc galaxies that do not undergo disc instability. To check the ability of the ELN-criterion to separate the two classes of disc galaxies to determine the presence or absence of instabilities, we tested its success rate. Effectively, we calculate the fraction of time spent by a galaxy in the bar unstable region according to the ELN-criterion (i.e., $\epsilon < 1.1$). The results showed that the ELN-criterion is able to detect bar formation in $\sim 75\%$ of the barred galaxies and correctly identifies the absence of a bar structure in $\sim 80\%$ of the unbarred galaxies. Despite the large success rate, we still find that the ELN-criterion fails in $\sim 25\%$ and $\sim 20\%$ of barred and unbarred galaxies, respectively. Carefully analyzing the properties of correctly and wrongly classified galaxies, we reach the following conclusions:

- While some differences exist in the disc mass and maximum circular velocities, the property in the ELN-criterion largely responsible for the correct or incorrect classification is the scale length of the disc: misclassified barred galaxies have a disc which is much more extended than the typical barred population. On the other hand, misclassified unbarred galaxies have small discs, similar to those of average barred galaxies. This seems to be related to the spin parameter of the halo, as we find a positive correlation between the value of the scale length and the spin parameter; less extended galaxies are hosted in more slowly spinning halos. This correlation, theoretically expected (see e.g., Fall & Efstathiou 1980; Mo et al. 1998b), was not present in the first simulations of disc galaxies (Scannapieco et al. 2009), but was retrieved in more recent simulation suites (Grand et al. 2017).

- Regarding unbarred galaxies misidentified by the ELN-criterion as potentially unstable, we found that their overall properties are similar to those of typical barred galaxies: at recent times, they are characterized by massive and compact discs with large stellar-to-halo ratios. However, the discs assemble later than those of barred galaxies, and the bulge components are significantly more prominent at early times than in barred galaxies. Moreover, the disc vertical scale length is generally larger than in barred galaxies, indicating hotter kinematics. We thus conclude that the bulge-to-disc ratio and/or the disc thickness should also be taken into account when determining disc stability.

• Concerning the population of barred galaxies that the ELN-criterion wrongly classifies as stable discs, we found that, they are generally much less compact than typical barred galaxies, and are embedded in dark matter halos with larger spin parameter. Interestingly, we also find that, at the epoch of bar formation, they may often have experienced a close encounter with a massive satellite. This might indicate that, for these galaxies, bar formation could be due to an external trigger, rather than being a consequence of the secular growth of the disc.

Given all the results summarized above, we can conclude that the Efstathiou et al. (1982) analytic criterion can robustly describe the stability of most secularly evolving massive disc galaxies. This has important implications for semi-analytic models of galaxy formation (SAMs) since, in most cases, the modelling of disc instability and the subsequent growth of the (pseudo)bulge component relies on the ELN-criterion. Thus, we argue that the predictions of current SAMs regarding massive barred galaxies in the local Universe can be trusted, at least to first order. Despite this, our analysis suggests that the criterion should be refined to take into account possible externally-induced instabilities or dependencies with the bulge-to-disc ratio. Thanks to the large volume provided by TNG100 and the high-resolution of TNG50, we plan to explore in future work different ways to include external triggers for bar formation in the ELN-criterion, to add extra dependencies that remove contamination and to apply these new criteria in semi-analytical models.

DATA AVAILABILITY

The IllustrisTNG simulations are publicly available and accessible at <https://www.tng-project.org/>. The catalogues of bars can be found in <https://www.tng-project.org/data/docs/specifications/>.

ACKNOWLEDGEMENTS

D.I.V acknowledge financial support provided under the European Union’s H2020 ERC Consolidator Grant “Binary Massive Black Hole Astrophysics” (B Massive, Grant Agreement: 818691) and INFN H45J18000450006. S.B. acknowledges partial support from the project PGC2018-097585-B-C22. YRG acknowledges the support of the “Juan de la Cierva Incorporation” fellowship (IJC2019-041131-I) and the European Research Council through grant number ERC-StG/716151. AL acknowledges support from MIUR under the grant PRIN 2017- MB8AEZ. The IllustrisTNG simulations were undertaken with compute time awarded by the Gauss Centre for Supercomputing (GCS) under GCS Large-Scale Projects GCS-ILLU and GCS-DWAR on the GCS share of the supercomputer Hazel Hen at the High Performance Computing Center Stuttgart (HLRS), as well as on the machines of the Max Planck Computing and Data Facility (MPCDF) in Garching, Germany.

REFERENCES

Abadi M. G., Navarro J. F., Steinmetz M., Eke V. R., 2003, *ApJ*, **597**, 21
 Aguerri J. A. L., Méndez-Abreu J., Corsini E. M., 2009, *A&A*, **495**, 491
 Algorry D. G., et al., 2017, *MNRAS*, **469**, 1054
 Athanassoula E., 2003, *MNRAS*, **341**, 1179
 Athanassoula E., 2008, *MNRAS*, **390**, L69
 Athanassoula E., Misiariotis A., 2002, *MNRAS*, **330**, 35
 Athanassoula E., Sellwood J. A., 1986, *MNRAS*, **221**, 213

Athanassoula E., Machado R. E. G., Rodionov S. A., 2013, *MNRAS*, **429**, 1949
 Barausse E., 2012, *MNRAS*, **423**, 2533
 Barazza F. D., Jogee S., Marinova I., 2008a, *ApJ*, **675**, 1194
 Barazza F. D., Jogee S., Marinova I., 2008b, *ApJ*, **675**, 1194
 Berentzen I., Athanassoula E., Heller C. H., Fricke K. J., 2004, *MNRAS*, **347**, 220
 Bonoli S., Mayer L., Kazantzidis S., Madau P., Bellovary J., Governato F., 2016, *MNRAS*, **459**, 2603
 Bullock J. S., Dekel A., Kolatt T. S., Kravtsov A. V., Klypin A. A., Porciani C., Primack J. R., 2001, *ApJ*, **555**, 240
 Bureau M., Freeman K. C., 1999, *AJ*, **118**, 126
 Cervantes Sodi B., 2017, *ApJ*, **835**, 80
 Cervantes-Sodi B., Li C., Park C., Wang L., 2013, *ApJ*, **775**, 19
 Cervantes Sodi B., Li C., Park C., 2015, *ApJ*, **807**, 111
 Collier A., Shlosman I., Heller C., 2018, *MNRAS*, **476**, 1331
 Combes F., 2009, in Jogee S., Marinova I., Hao L., Blanc G. A., eds, *Astronomical Society of the Pacific Conference Series Vol. 419, Galaxy Evolution: Emerging Insights and Future Challenges*. p. 31 ([arXiv:0901.0178](https://arxiv.org/abs/0901.0178))
 Comerón S., et al., 2011, *ApJ*, **741**, 28
 Cora S. A., et al., 2018, *MNRAS*, **479**, 2
 Croton D. J., et al., 2016, *ApJS*, **222**, 22
 Davé R., Anglés-Alcázar D., Narayanan D., Li Q., Rafieferantsoa M. H., Appleby S., 2019, *MNRAS*, **486**, 2827
 Davis M., Efstathiou G., Frenk C. S., White S. D. M., 1985, *ApJ*, **292**, 371
 DeBuhr J., Ma C.-P., White S. D. M., 2012, *MNRAS*, **426**, 983
 Debattista V. P., Sellwood J. A., 1998, *ApJ*, **493**, L5
 Debattista V. P., Sellwood J. A., 2000, *ApJ*, **543**, 704
 Díaz-García S., Salo H., Laurikainen E., Herrera-Endoqui M., 2016, *A&A*, **587**, A160
 Du M., Ho L. C., Zhao D., Shi J., Debattista V. P., Hernquist L., Nelson D., 2019, *ApJ*, **884**, 129
 Dubinski J., Berentzen I., Shlosman I., 2009, *ApJ*, **697**, 293
 Dubois Y., Volonteri M., Silk J., 2014, *MNRAS*, **440**, 1590
 Efstathiou G., Lake G., Negroponte J., 1982, *MNRAS*, **199**, 1069
 Eskridge P. B., et al., 2000, *AJ*, **119**, 536
 Fall S. M., Efstathiou G., 1980, *MNRAS*, **193**, 189
 Fragkoudi F., Di Matteo P., Haywood M., Gómez A., Combes F., Katz D., Semelin B., 2017, *A&A*, **606**, A47
 Fragkoudi F., Grand R. J. J., Pakmor R., Springel V., White S. D. M., Marinacci F., Gomez F. A., Navarro J. F., 2021, *A&A*, **650**, L16
 Frankel N., et al., 2022, *arXiv e-prints*, p. [arXiv:2201.08406](https://arxiv.org/abs/2201.08406)
 Fraser-McKelvie A., et al., 2020, *MNRAS*, **499**, 1116
 Gadotti D. A., 2009, *MNRAS*, **393**, 1531
 Gao L., White S. D. M., 2007, *MNRAS*, **377**, L5
 Gargiulo I. D., et al., 2021, *arXiv e-prints*, p. [arXiv:2111.13712](https://arxiv.org/abs/2111.13712)
 Gavazzi G., et al., 2015, *A&A*, **576**, A16
 Genel S., Fall S. M., Hernquist L., Vogelsberger M., Snyder G. F., Rodriguez-Gomez V., Sijacki D., Springel V., 2015, *ApJ*, **804**, L40
 Ghosh S., Saha K., Di Matteo P., Combes F., 2021, *MNRAS*, **502**, 3085
 Grand R. J. J., et al., 2017, *MNRAS*, **467**, 179
 Grosbøl P., Patsis P. A., Pompei E., 2004, *A&A*, **423**, 849
 Guedes J., Madau P., Mayer L., Callegari S., 2011, *ApJ*, **729**, 125
 Guo Q., et al., 2011, *MNRAS*, **413**, 101
 Holley-Bockelmann K., Weinberg M., Katz N., 2005, *MNRAS*, **363**, 991
 Irodotou D., Thomas P. A., Henriques B. M., Sargent M. T., Hislop J. M., 2019, *MNRAS*, **489**, 3609
 Izquierdo-Villalba D., Bonoli S., Spinoso D., Rosas-Guevara Y., Henriques B. M. B., Hernández-Monteagudo C., 2019, *MNRAS*, **488**, 609
 Jiang F., et al., 2019, *MNRAS*, **488**, 4801
 Kalnajs A. J., 1972, *ApJ*, **175**, 63
 Kataria S. K., Das M., 2018, *MNRAS*, **475**, 1653
 Kataria S. K., Das M., Barway S., 2020, *A&A*, **640**, A14
 Knapen J. H., 1999, in Beckman J. E., Mahoney T. J., eds, *Astronomical Society of the Pacific Conference Series Vol. 187, The Evolution of Galaxies on Cosmological Timescales*. pp 72–87 ([arXiv:astro-ph/9907290](https://arxiv.org/abs/astro-ph/9907290))

- Kormendy J., 1993, in Dejonghe H., Habing H. J., eds, IAU Symposium Vol. 153, Galactic Bulges. p. 209
- Kormendy J., Ho L. C., 2013, *ARA&A*, 51, 511
- Lacey C. G., et al., 2016, *MNRAS*, 462, 3854
- Lagos C. d. P., Tobar R. J., Robotham A. S. G., Obreschkow D., Mitchell P. D., Power C., Elahi P. J., 2018, *MNRAS*, 481, 3573
- Lokas E. L., Athanassoula E., Debattista V. P., Valluri M., Pino A. d., Semczuk M., Gajda G., Kowalczyk K., 2014, *MNRAS*, 445, 1339
- Long S., Shlosman I., Heller C., 2014, *ApJ*, 783, L18
- Lynden-Bell D., Kalnajs A. J., 1972, *MNRAS*, 157, 1
- Marinacci F., Pakmor R., Springel V., 2014, *MNRAS*, 437, 1750
- Marinacci F., et al., 2018, *MNRAS*, 480, 5113
- Marioni O. F., Abadi M. G., Gottlöber S., Yepes G., 2022, *MNRAS*,
- Marshall M. A., Mutch S. J., Qin Y., Poole G. B., Wyithe J. S. B., 2019, *MNRAS*, 488, 1941
- Mayer L., Wadsley J., 2004, *MNRAS*, 347, 277
- Menéndez-Delmestre K., Sheth K., Schinnerer E., Jarrett T. H., Scoville N. Z., 2007, *ApJ*, 657, 790
- Miwa T., Noguchi M., 1998, *ApJ*, 499, 149
- Mo H. J., Mao S., White S. D. M., 1998a, *MNRAS*, 295, 319
- Mo H. J., Mao S., White S. D. M., 1998b, *MNRAS*, 295, 319
- Moetzedian R., Polyachenko E. V., Berczik P., Just A., 2017, *A&A*, 604, A75
- Naiman J. P., et al., 2018, *MNRAS*, 477, 1206
- Navarro J. F., Benz W., 1991, *ApJ*, 380, 320
- Navarro J. F., Steinmetz M., 2000, *ApJ*, 538, 477
- Nelson D., et al., 2018, *MNRAS*, 475, 624
- Nelson D., et al., 2019a, *Computational Astrophysics and Cosmology*, 6, 2
- Nelson D., et al., 2019b, *MNRAS*, 490, 3234
- Ostriker J. P., Peebles P. J. E., 1973, *ApJ*, 186, 467
- Peschken N., Lokas E. L., 2019, *MNRAS*, 483, 2721
- Pfenniger D., Norman C., 1990, *ApJ*, 363, 391
- Pillepich A., et al., 2018a, *MNRAS*, 473, 4077
- Pillepich A., et al., 2018b, *MNRAS*, 475, 648
- Pillepich A., et al., 2019, *MNRAS*, 490, 3196
- Planck Collaboration et al., 2016, *A&A*, 594, A13
- Reddish J., et al., 2021, arXiv e-prints, p. arXiv:2106.02622
- Rodríguez-Gomez V., et al., 2015, *MNRAS*, 449, 49
- Romano-Díaz E., Shlosman I., Heller C., Hoffman Y., 2008, *ApJ*, 687, L13
- Romeo A. B., Agertz O., Renaud F., 2022, arXiv e-prints, p. arXiv:2204.02695
- Rosas-Guevara Y., et al., 2020, *MNRAS*, 491, 2547
- Rosas-Guevara Y., et al., 2021, arXiv e-prints, p. arXiv:2110.04537
- Roshan M., Ghafourian N., Kashfi T., Banik I., Haslbauer M., Cuomo V., Famaey B., Kroupa P., 2021, *MNRAS*, 508, 926
- Saha K., Gerhard O., 2012, arXiv e-prints, p. arXiv:1212.4579
- Saha K., Naab T., 2013, *MNRAS*, 434, 1287
- Sakamoto K., Okumura S. K., Ishizuki S., Scoville N. Z., 1999, *ApJ*, 525, 691
- Scannapieco C., White S. D. M., Springel V., Tissera P. B., 2009, *MNRAS*, 396, 696
- Scannapieco C., White S. D. M., Springel V., Tissera P. B., 2011, *MNRAS*, 417, 154
- Schaye J., et al., 2015, *MNRAS*, 446, 521
- Schwarz M. P., 1981, *ApJ*, 247, 77
- Sellwood J. A., 1980, *A&A*, 89, 296
- Sellwood J. A., Evans N. W., 2001, *ApJ*, 546, 176
- Sersic J. L., 1968, Atlas de Galaxias Australes
- Shen S., Mo H. J., White S. D. M., Blanton M. R., Kauffmann G., Voges W., Brinkmann J., Csabai I., 2003, *MNRAS*, 343, 978
- Sheth K., et al., 2010, *PASP*, 122, 1397
- Sheth K., Melbourne J., Elmegreen D. M., Elmegreen B. G., Athanassoula E., Abraham R. G., Weiner B. J., 2012, *ApJ*, 758, 136
- Spinoso D., Bonoli S., Dotti M., Mayer L., Madau P., Bellovary J., 2017, *MNRAS*, 465, 3729
- Springel V., 2005, *MNRAS*, 364, 1105
- Springel V., 2010, *MNRAS*, 401, 791
- Springel V., White S. D. M., Tormen G., Kauffmann G., 2001, *MNRAS*, 328, 726
- Springel V., et al., 2018, *MNRAS*, 475, 676
- Toomre A., 1981, in Fall S. M., Lynden-Bell D., eds, Structure and Evolution of Normal Galaxies. pp 111–136
- Tremaine S., Weinberg M. D., 1984, *ApJ*, 282, L5
- Valenzuela O., Klypin A., 2003, *MNRAS*, 345, 406
- Vogelsberger M., et al., 2014a, *MNRAS*, 444, 1518
- Vogelsberger M., et al., 2014b, *Nature*, 509, 177
- Weinberg M. D., Katz N., 2007a, *MNRAS*, 375, 425
- Weinberg M. D., Katz N., 2007b, *MNRAS*, 375, 460
- Weinberger R., et al., 2017, *MNRAS*, 465, 3291
- Yang H., Gao L., Frenk C. S., Grand R. J. J., Guo Q., Liao S., Shao S., 2021, arXiv e-prints, p. arXiv:2110.04434
- Yoachim P., Dalcanton J. J., 2006, *AJ*, 131, 226
- Yurin D., Springel V., 2015, *MNRAS*, 452, 2367
- Zana T., Dotti M., Capelo P. R., Bonoli S., Haardt F., Mayer L., Spinoso D., 2018a, *MNRAS*, 473, 2608
- Zana T., Dotti M., Capelo P. R., Mayer L., Haardt F., Shen S., Bonoli S., 2018b, *MNRAS*, 479, 5214
- Zana T., Capelo P. R., Dotti M., Mayer L., Lupi A., Haardt F., Bonoli S., Shen S., 2019, *MNRAS*, 488, 1864
- Zhou Z.-B., Zhu W., Wang Y., Feng L.-L., 2020, arXiv e-prints, p. arXiv:2004.11620
- van Albada G. D., Roberts W. W. J., 1981, *ApJ*, 246, 740

APPENDIX A: THE DISC SCALE LENGTH FROM A KINEMATICS DECOMPOSITION

In this appendix we compare our values of the disc scale length, R_d , with the ones computed based on a kinematics decomposition, R_d^{kin} . In particular, the latter has been computed making use of the morphological classification of Zana et al. (submitted) which, based on the particle kinematics, is capable of distinguishing for any galaxy 5 different components: thin disc, thick disc, bulge, pseudobulge and stellar halo. By selecting only *thin disc particles*, we have performed an exponential fit to the resulting face-on surface density profile, $\Sigma_{\text{stars}}(r)$ (see second term of Eq. 6). In Fig. A1 we present the ratio between R_d and R_d^{kin} for 5 random galaxies in the BUR, BSR, UBUR and UBSR TNG100 sample As shown, for all the cases the ratio varies around 1, with few cases where R_d/R_d^{kin} is outside the range 0.75 to 1.25.

This paper has been typeset from a $\text{\TeX}/\text{\LaTeX}$ file prepared by the author.

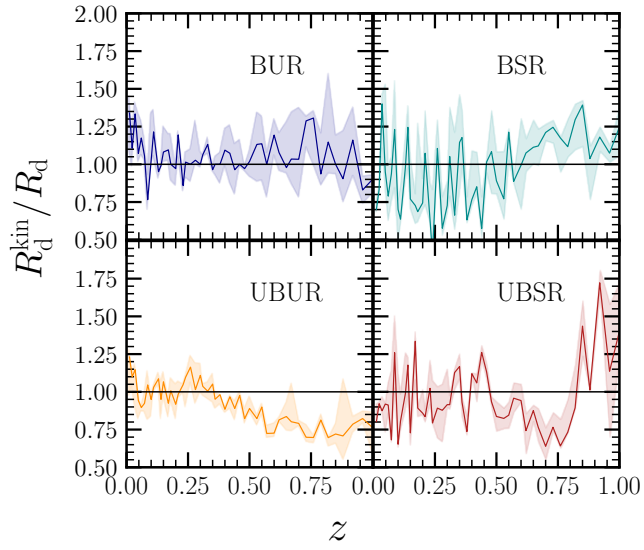


Figure A1. Ratio between the scale length computed by fitting the mass surface density of thin disc particles (R_d^{kin}) and the scale length computed according to Section 2.2 (R_d). Solid line represents the median whereas the shaded area displays the 32th – 68th percentile. Dark blue, cyan, orange and red lines are the results for BUR, BSR, UBUR and UBSR TNG100 samples.